Remote Sensing of Environment 291 (2023) 113559

Contents lists available at ScienceDirect

Remote Sensing of Environment

journal homepage: www.elsevier.com/locate/rse

Constraining industrial ammonia emissions using hyperspectral infrared imaging

Lara Noppen [a,*], Lieven Clarisse [a], Frederik Tack [b], Thomas Ruhtz [c], Alexis Merlaud [b], Martin Van Damme [a,b], Michel Van Roozendael [b], Dirk Schuettemeyer [d], Pierre Coheur [a]

[a] Université libre de Bruxelles (ULB), Spectroscopy, Quantum Chemistry and Atmospheric Remote Sensing (SQUARES), Brussels, Belgium
[b] Royal Belgian Institute for Space Aeronomy (BIRA-IASB), Brussels, Belgium
[c] Freie Universität Berlin, Berlin, Germany
[d] European Space Agency (ESA-ESTEC), Noordwijk, The Netherlands

ARTICLE INFO

Edited by Menghua Wang

Keywords:
Hyperspectral infrared
Aircraft measurements
Emission fluxes
Ammonia
Nitrogen dioxide
Fertilizer production
Soda ash
Nitrosat

ABSTRACT

Atmospheric emissions of reactive nitrogen in the form of nitrogen dioxide (NO_2) and ammonia (NH_3) worsen air quality and upon deposition, dramatically affect the environment. Recent infrared satellite measurements have revealed that NH_3 emitted by industries are an important and underestimated emission source. Yet, to assess these emissions, current satellite sounders are severely limited by their spatial resolution. In this paper, we analyse measurement data recorded in a series of imaging surveys that were conducted over industries in the Greater Berlin area (Germany). On board the aircraft were the Telops Hyper-Cam LW, targeting NH_3 measurements in the longwave infrared at a resolution of 4 m and the SWING+ spectrometer targeting NO_2 measurements in the UV–Vis at a resolution of 180 m.

Two flights were carried out over German's largest production facility of synthetic NH_3, urea and other fertilizers. In both cases, a large NH_3 plume was observed originating from the factory. Using a Gaussian plume model to take into account plume rise and dispersion, coupled with well-established radiative transfer and inverse methods, we retrieve vertical column densities. From these, we calculate NH_3 emission fluxes using the integrated mass enhancement and cross-sectional flux methods, yielding consistent emissions of the order of 2200 t yr^{-1} for both flights, assuming constant fluxes across the year. These estimates are about five times larger than those reported in the European Pollutant Release and Transfer Register (E-PRTR) for this plant. In the second campaign, a co-emitted NO_2 plume was measured, likely related to the production of nitric acid at the plant.

A third flight was carried out over an area comprising the cities of Staßfurt and Bernburg. Several small NH_3 plumes were seen, one over a production facility of mineral wool insulation, one over a sugar factory and two over the soda ash plants in Staßfurt and Bernburg. A fifth and much larger plume was seen to originate from the sedimentation basins associated with the soda ash plant in Staßfurt, indicating rapid volatilization of ammonium rich effluents. We use the different measurement campaigns to simulate measurements of Nitrosat, a potential future satellite sounder dedicated to the sounding of reactive nitrogen at a resolution of 500 m. We demonstrate that such measurements would allow accurately constraining emissions in a single overpass, overcoming a number of important drawbacks of current satellite sounders.

1. Introduction

The two principal forms of reactive nitrogen (Nr) emitted to the atmosphere are nitrogen dioxide (NO_2) and ammonia (NH_3). Tropospheric nitrogen oxides are emitted from fossil fuel combustion, vegetation fires, soil and lightning (Stavrakou et al., 2013). NH_3 is emitted into the atmosphere from biomass burning, oceans, soils, wild animals, industries, waste water treatment, fossil fuel combustion and domestic activities (Battye et al., 1994; Behera et al., 2013; Bouwman et al., 1997; Bray et al., 2018). The main source of NH_3 however, is agriculture (Sutton et al., 2013), which accounts for more than 80% of the total emissions in Europe (Pinterits et al., 2020), the United States (Bray et al., 2018) and China (Zhang et al., 2017). An important role is played by NH_3-based fertilizers, which are synthesized on a massive industrial scale, supporting the world's need for food and

* Corresponding author.
E-mail address: lara.noppen@ulb.be (L. Noppen).

https://doi.org/10.1016/j.rse.2023.113559
Received 6 October 2022; Received in revised form 2 February 2023; Accepted 28 March 2023
Available online 10 April 2023

feed (Erisman et al., 2008; Galloway et al., 2008). A large part of this produced NH_3 is lost to the atmosphere, through volatilization from synthetic fertilizer application and losses from livestock waste (Erisman et al., 2015).

Anthropogenic emissions of Nr strongly perturb the global nitrogen cycle, with devastating consequences for the environment. Deposition leads to a reduction of biodiversity through eutrophication and acidification of water and soils (Aneja et al., 2001; Dise et al., 2011; Erisman et al., 2013). Both NO_2 and NH_3 also contribute to the formation of particulate matter, deteriorating air quality, human health and life expectancy (Erisman et al., 2013; Lelieveld et al., 2015; Pope et al., 2009). While NO_2 emissions are declining worldwide (Georgoulias et al., 2019), atmospheric NH_3 levels are still increasing in most countries, with a recent study estimating increases of about 2% per year in Europe and the United States and 6% per year in East Asia (Van Damme et al., 2021). The issue is making its way on the international political agenda, but to successfully reduce worldwide NH_3 emissions and their environmental impacts, it is imperative that legislative action is supported by effective monitoring means.

Satellite observations of NH_3 have now become widely available, allowing analysis of the entire global atmospheric distribution of NH_3 and its temporal variability (e.g. Hickman et al. (2021), Shephard et al. (2020), Van Damme et al. (2021), Wang et al. (2021)). Using model assimilation and inversion, satellite data is being used to estimate regional and global NH_3 emission and deposition budgets (e.g. Chen et al. (2021), Evangeliou et al. (2021), Kharol et al. (2018)). Other satellite-derived work relates to the study of individual NH_3 sources, such as animal farms and chemical fertilizer plants. To overcome the rather coarse spatial resolution (≥12 km) of the spaceborne Infrared Atmospheric Sounding Interferometer (IASI), Van Damme et al. (2018) exploited long term averages, and were able to identify and quantify the world's largest point emitters. They highlighted the importance of these on a global scale, and the fact that their emissions are significantly underestimated in state of the art bottom-up inventories. Follow-up work increased the number of identified global point sources to about 500 (Clarisse et al., 2019b) and estimated the atmospheric lifetime of NH_3 on a per site basis (Dammers et al., 2019). Despite the obvious progress that has been made, it has become clear that the limits are being reached on what can be done with existing satellite sounders. Indeed, their spatial resolution is much coarser than the typical size of an NH_3 point source, which makes the measurement of their emissions very challenging. Only the most important and isolated sources could be identified from space measurements and many smaller point sources, especially farms, were missed. Therefore, an effective monitoring of a species with a temporal and spatial variability as large as that of NH_3 requires an instrument capable of measuring at a much smaller spatial scale than that of IASI and other current hyperspectral infrared sounders.

It is in this context that a new satellite, called Nitrosat,[1] has been proposed in answer to the 11th Earth Explorer Call from the European Space Agency (ESA). Nitrosat aims at mapping Nr on a global scale by measuring NO_2 and NH_3 in gapless swaths of over 80 km at a spatial resolution of 500 m or below. This satellite would be launched in 2031 and would have a lifetime of at least three years. During this time frame, Nitrosat would observe the Earth simultaneously with other European missions such as CO2M, Sentinel 4 and Sentinel 5. All these missions are complementary and will provide improved measurements of NO_2 and NH_3, but none of them will come close to the spatial resolution provided by Nitrosat (Coheur et al., 2021).

In 2021, Nitrosat was selected to enter phase 0 (pre-development). To support the proposal and demonstrate what this satellite mission could offer, ESA is currently funding aircraft campaigns, called Nitrocam. Each flight aims at mapping NO_2 and NH_3 in an area of at least 10 by 15 km and across different source areas in Europe. The instruments on board are the UV–Vis SWING+ spectrometer developed by the Royal Belgian Institute for Space Aeronomy (BIRA-IASB) for observing NO_2 at a spatial resolution of about 180 m (Merlaud et al., 2018) and the commercial Telops infrared Hyper-Cam LW instrument, owned by German Research Center for Geosciences (GFZ), targeting NH_3 at a resolution of 4 m (Telops, 2022).

The present paper reports the results of a first series of Nitrocam flights over industries in the Greater Berlin area (Germany), with a focus on deriving industrial NH_3 emission rates. In the next section, we present the data measured in autumn 2020 over a fertilizer production facility in Piesteritz. An approach based on a hyperspectral range index (HRI) is used to detect the NH_3 plume emitted by the plant and its emission rates are derived using different complementary approaches. This includes a simulation of the measurements as they would be observed by Nitrosat. In Section 3, we report on two flights that took place in spring 2021, one over the same fertilizer plant of Piesteritz and the other over different types of industry near the cities of Staßfurt and Bernburg. In the last section we discuss the results in a wider context and summarize the main conclusions.

2. NH_3 measured by Hyper-Cam LW over Piesteritz in autumn 2020

The first Nitrocam flight took place on 8 October, 2020, between 10 and 11 AM (local time) near Piesteritz, Germany (51.88°N, 12.58°E), over an area of $\sim 10 \times 15$ km^2 as shown in Fig. 1a. The target of the campaign was the Piesteritz fertilizer plant. It is the largest German production facility of NH_3 and urea, with a yearly production capacity over 1200 kt for both compounds (European Commission, 2007). The factory was earlier identified as an emission hotspot of atmospheric NH_3 (Clarisse et al., 2019b), and serves as a representative example of the main type of industrial NH_3 emitter.

For this flight, only the Hyper-Cam LW was operational. The Hyper-Cam LW (Lagueux et al., 2009a,b; Montembeault et al., 2010) is an imaging Fourier interferometer operating in the longwave infrared between 800 and 1350 cm^{-1}. Observing in nadir geometry, it combines a very high spatial resolution (4 m) with a medium spectral sampling (1.65 cm^{-1}). The instrument was mounted on the Telops' airborne platform and transported by the Cessna T207A aircraft to an altitude of 3 km. The area was surveyed by means of parallel, slightly overlapping swaths of about 1 km wide.

For each observation, we calculated the median brightness temperature over all spectral channels between 850 and 1100 cm^{-1}. The distribution of these temperatures is presented in Fig. 1b. Notable features are: the Elbe river, at a temperature around 286 K, slightly warmer than the surrounding fields, some very small clouds in the north-east and solar panels west from the industrial site, featuring brightness temperatures below 278 K. During the flight, the soil temperature increased several degrees, which can be seen from the west-to-east temperature gradient in the distribution.

2.1. Detection of NH_3

To attempt to detect NH_3 in the observed spectra, we used the so-called HRI or matched filter method, a close-to-optimal detection technique widely used both for NH_3 satellite observations (Whitburn et al., 2016), and hyperspectral imaging applications (Manolakis et al., 2016). The HRI is a dimensionless variable that quantifies the strength of the signal of a target compound (NH_3 in our case) in an observed spectrum, accounting for the expected spectral variability due to noise and the state of the surface and atmosphere. It can be interpreted as

[1] https://www.esa.int/Applications/Observing_the_Earth/FutureEO/Preparing_for_tomorrow/Four_mission_ideas_to_compete_for_Earth_Explorer_11.

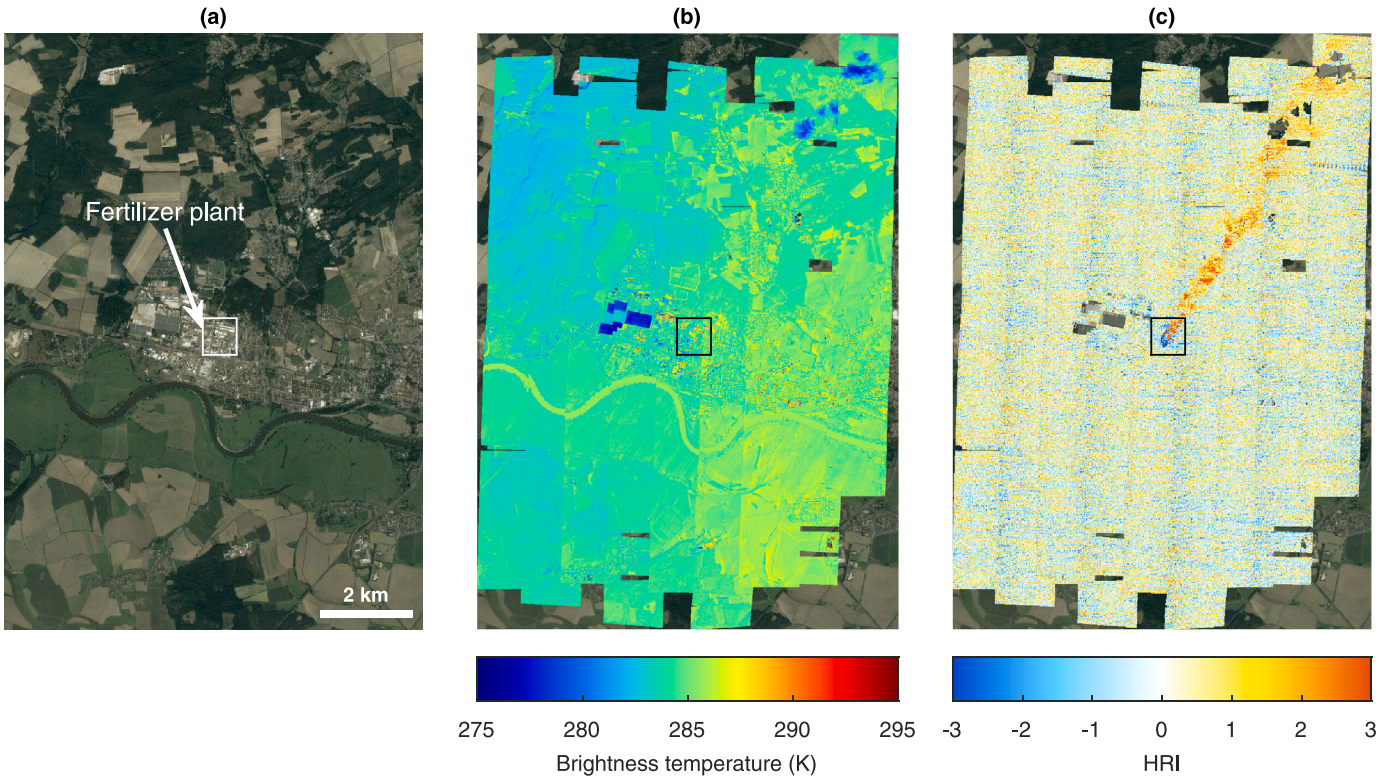

Fig. 1. (a) Satellite visible imagery from Google Maps of the overflown area on 8 October 2020, centred on the fertilizer plant of Piesteritz (Germany). (b) Distribution of the median brightness temperature of each spectrum. (c) NH_3 HRI distribution at 12 m resolution revealing a plume originating from the fertilizer plant. The boxes correspond to the area shown in Fig. 2.

a generalized signal-to-noise ratio and is calculated, for each observed spectrum y, as:

$$\mathrm{HRI} = \frac{K^T S_y^{-1}(y-\bar{y})}{\sqrt{K^T S_y^{-1} K}} \quad (1)$$

with $\bar{y}$ and S_y respectively the mean and covariance matrix of a representative set of spectra containing background quantities of NH_3. K is the Jacobian of NH_3, calculated as the difference between two spectra with different quantities of NH_3. By definition, the HRI has an average of zero and a standard deviation of one on background spectra. If the underlying distribution is normal, the HRI behaves like a z-score, where a value above three indicates a probability higher than 0.99 that an enhanced NH_3 signature is present in the spectrum. In practice, however, the distribution is rarely perfectly normal, and outliers are common. When in doubt, a more robust spectral verification in the form of spectral fitting or spectral whitening (De Longueville et al., 2021) is called for. In what follows, we calculated the HRI in the 900–1000 cm^{-1} spectral range, where the strongest NH_3 absorption features are located.

For the calculation of the mean spectrum and its associated covariance matrix, we used a recursive approach where first the mean and covariance matrix are calculated on all spectra. This allows the calculation of a preliminary HRI and removal of spectra containing enhanced signatures of NH_3. Then, from the remaining spectra, a second and final mean and covariance matrix are calculated (Clarisse et al., 2019a). To reduce noise, we present here mostly averaged HRI distributions (e.g. averaging 3 × 3 pixels yields a spatial distribution at 12 m resolution, with a factor three improvement in the signal-to-noise). In these distributions, the HRI is scaled in such a way that a standard deviation of one is obtained over the background, so that the HRI keeps its usual interpretation in terms of the z-score.

As shown in Fig. 1c, the distribution of the NH_3 HRI obtained in this way reveals a large plume of NH_3 originating from the industrial plant and extending over 7 km in the north-east direction. The spectra measured over the solar panels were filtered out based on the median brightness temperature (removing observations below 282 K), as they led to false detections due to sharp emissivity features in the spectral range of interest. This filter also served to remove the observations over clouds. Apart from the main plume, which will be discussed in detail further in the manuscript, large HRI values are found directly over the industrial complex (Fig. 2c). Both large positive and large negative HRIs are seen, respectively indicating dominant absorption and emission of infrared radiation by NH_3. Note that for the calculation of the HRI, we used a Jacobian that shows NH_3 in absorption hence from Eq. (1), NH_3 in absorption will result in a positive HRI while emission in a negative one.

Examples of (averaged) spectra from both classes are shown in blue in panels (d) and (e) of Fig. 2. These panels also display fitted synthetic spectra (in red) obtained with a fitting model that adjusts the surface temperature and the concentrations of the atmospheric constituents to best match the observed spectrum (see next section). The differences between the two (shown in green) have root mean squares values (RMS) of 0.1 and 0.3 K. Withholding NH_3 from the fit leads to a residual (orange) with large features of NH_3 around 930 and 965 cm^{-1} (black) apparent in both the absorption (−3 K) and emission (7 K) spectrum, thereby unambiguously confirming the presence of NH_3. The same exercise was repeated for spectra within the downwind plume, confirming also here the HRI detection of NH_3.

Whether NH_3 is observed in absorption or emission depends on the temperature difference between the background radiation (surface) and the temperature of the NH_3 plume. This difference is more generally known as the thermal contrast. With satellites, NH_3 is usually observed in absorption during daytime, and in emission during nighttime when thermal inversion is common (Clarisse et al., 2010, 2021). In the scene under consideration, the differences in thermal contrast are largely driven by the temperature of the different buildings and surface materials. This becomes clear when we compare the HRI distribution (Fig. 2c)

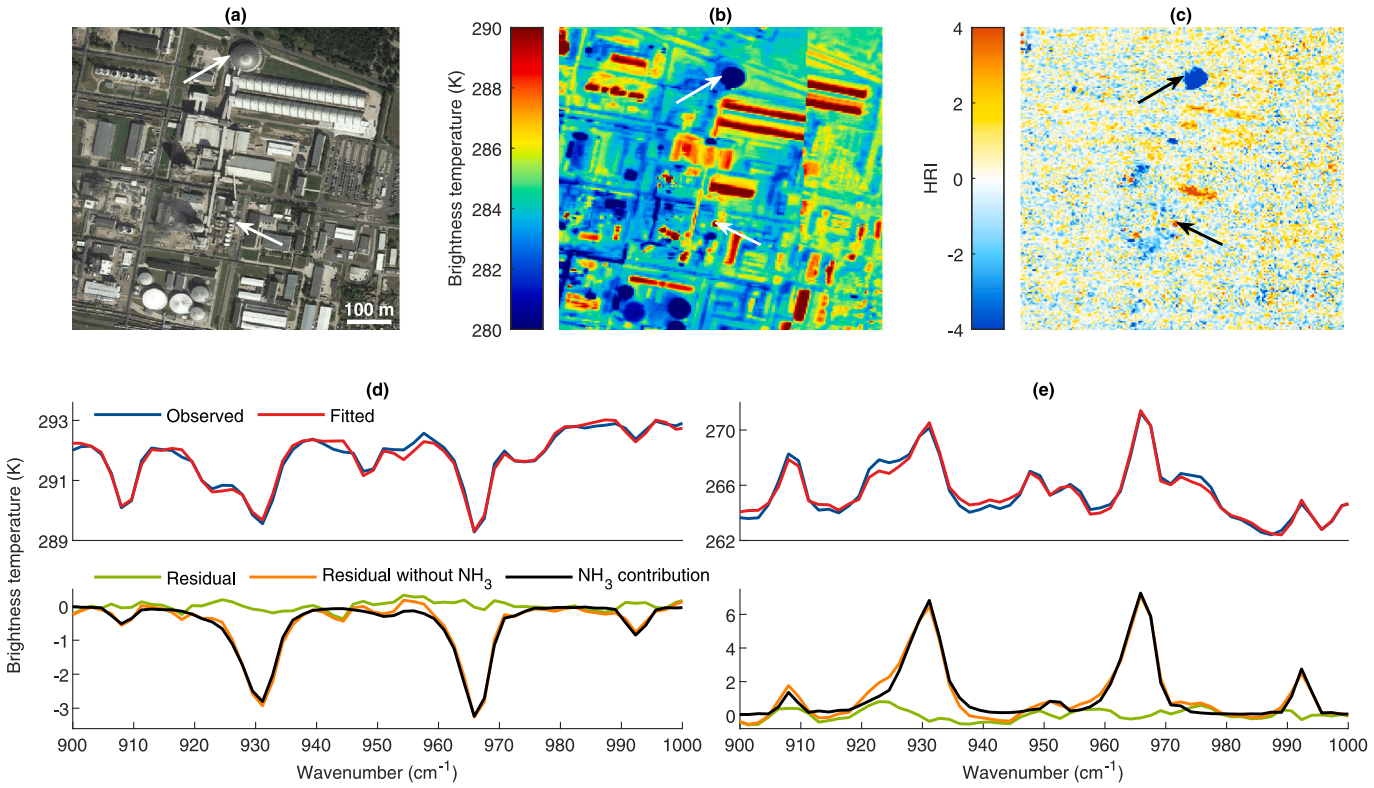

Fig. 2. Close-up views over the industrial site of (a) the satellite visible imagery from Google Maps, (b) the distribution of the brightness temperatures and (c) the HRI distribution from Fig. 1. Absorption and emission spectra averaged in the zones marked by arrows on the top panels are shown in panels (d) and (e). Observed spectra are shown in blue and the fitted ones in red. The differences between observed and fitted spectra (green) are displayed in the bottom panels. The residuals without NH_3 (orange) are obtained by subtracting the NH_3 contributions (black) from the simulations. (For interpretation of the references to colour in this figure legend, the reader is referred to the web version of this article.)

with that of the temperature (Fig. 2b), and a Google Earth photograph of the corresponding area (Fig. 2a). Large positive HRIs can be discerned over several hot rooftops, whereas negative HRIs are observed over much colder storage tanks or silos. Note that thermal contrast not only determines the sign of the NH_3 signature, it also affects sensitivity of the observations to the target species, as a higher thermal contrast (in absolute value) leads to larger spectral signatures. This is particularly important for species located close to the surface (Bauduin et al., 2017), and is important for the discussion of the results in the next section.

The high spatial resolution of Hyper-Cam LW allows downsampling the measurements to various hypothetical satellite footprints as illustrated in Fig. 3 that shows HRI distributions computed at 200, 500 and 2000 m. The 200 and 500 m resolutions result in larger mean HRIs compared to the native measurements, allowing for a better visualization of the plume. For larger pixels, the plume becomes increasingly more dilute, and more difficult to attribute to the source. The resolution of 500 m shown on panel (b) corresponds to the resolution proposed for the Nitrosat candidate mission. While some of the finer detail is lost, at 500 m the plume can be seen with a good degree of spatial detail, enabling a straightforward identification of its source. This is immediately also the first demonstration that Nitrosat could measure, in a single overpass, an entire industrial plume of NH_3. In the next sections we show further that meaningful NH_3 concentrations and emission fluxes can be derived from such measurements.

2.2. Quantification of NH_3

To retrieve NH_3 vertical column densities from the measurements, we employed the optimal estimation method as implemented in the line-by-line radiative transfer code Atmosphit (Barret et al., 2005). The method iteratively minimizes the difference between the observed and the fitted spectrum (Rodgers, 2000), by adjusting the state of the surface and atmosphere, and allows simultaneously for the use of a priori information. The fitting range was set between 900 and 1000 cm^{-1}. NH_3 was given an a priori peak concentration of 200 ppb (450 ppb for the CSF-200 m retrieval for the non-rising plume, see the scenarios descriptions below) and a lose fitting constraint corresponding to 500% variability. The surface temperature, and total columns of water vapour (H_2O), ozone (O_3) and carbon dioxide (CO_2) were fitted with a variability of 30%. For the different species, total columns were fitted by uniformly scaling the a priori vertical profile. Vertical profiles of temperature, pressure and gas concentrations (except for NH_3, see below) were derived from ERA5 data from the European Centre for Medium-Range Weather Forecasts (Hersbach et al., 2020) and standard atmospheric models (Kneizys et al., 1996). For the radiative transfer calculations, the atmosphere was divided into 35 homogeneous layers between 0 and 3 km.

In what follows, we focus on the downwind plume, as retrievals over the factory itself are complicated by the large temperature gradients, inhomogeneous surface emissivities and the unknown temperature of the NH_3 gas close to the chimneys. For the downwind plume we assume a plume temperature equal to the ambient temperature. Mainly for computational reasons, rather than fitting each individual spectrum, we averaged the plume in 10 sections as shown in Fig. 4, leading to a reduction in spectral noise by a factor ~60 to 200 over a single spectrum.

Through the sensitivity to thermal contrast, the retrieval of the total column of NH_3 is dependent on the assumed plume altitude. As we cannot extract such information directly from the spectra (Clarisse et al., 2010), assumptions need to be made. Using a common plume model as detailed in Appendix, we consider two realistic, but contrasting scenarios. One of a non-rising plume (orange in Fig. 5a) and one of a

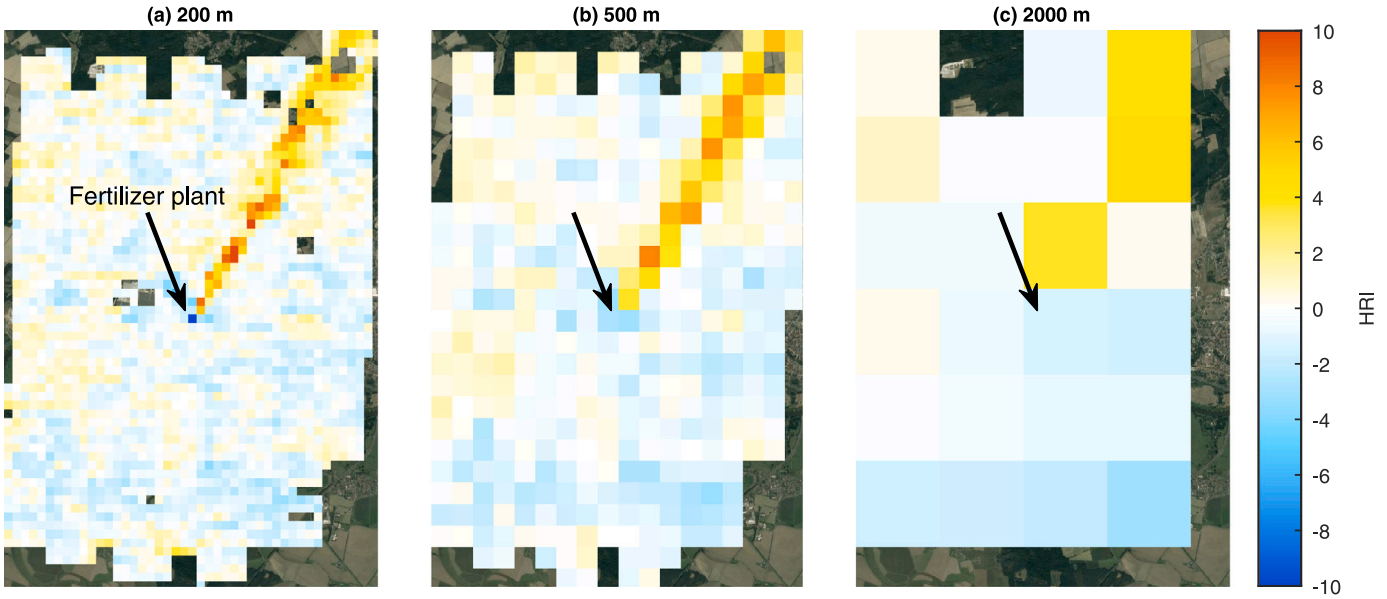

Fig. 3. NH_3 HRI distributions computed at spatial resolutions of (a) 200 m, (b) 500 m and (c) 2000 m centred on the fertilizer plant of Piesteritz (marked by an arrow on each panel) from the native data shown in Fig. 1c.

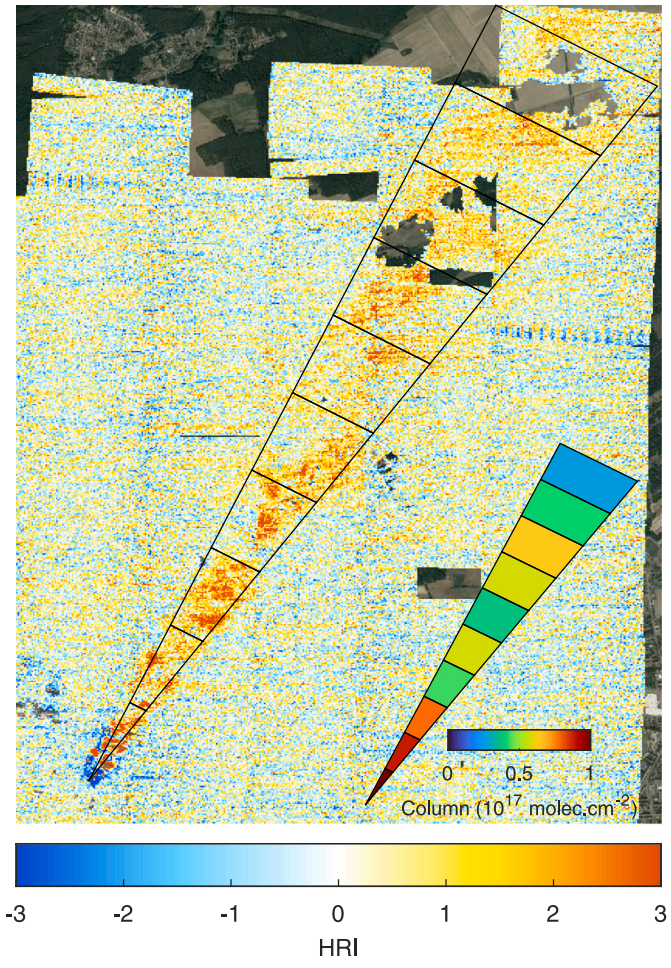

Fig. 4. Close-up of the NH_3 HRI distribution at 12 m resolution of Fig. 1c, illustrating the partitioning of the plume in 10 sections. In the bottom right corner of the figure are the NH_3 columns retrieved with the CSF method for the rising plume scenario displayed in blue in Fig. 5.

buoyant plume (blue in Fig. 5a). Both plumes are assumed to undergo vertical mixing at a rate typical for a stable atmosphere.

The 10 average spectra corresponding to the trapezoids in Fig. 4 were fitted assuming both of these profiles. The quality of the fits, with RMS values between 0.02 and 0.03 K, are even better than those shown in Fig. 2 since more spectra are averaged. From each column, a background column of 2.9 10^{15} molec cm^{-2} was subtracted, which was estimated independently from the mean of spectra measured outside of the plume. The resulting columns are shown in Fig. 5b and are seen to decrease with the distance from the source. This is logical as the plume disperses downwind over a larger area and as columns are expressed per surface unit. The large difference between the columns retrieved in the two scenarios originates from the dependence of the thermal contrast with the altitude: for a given quantity of NH_3, more thermal contrast leads to a larger spectral signature, and conversely, for a given spectral signature, assuming a larger thermal contrast/higher altitude in the retrieval, results in lower retrieved columns. Note that the retrieval uncertainty is larger at lower than at higher altitude, as in that case small uncertainties in the thermal contrast (e.g. due to small biases in the ERA5 temperature profiles) are relatively more important. This likely contributes to the larger fluctuations of the retrieved columns along the line of transport in the first scenario.

2.3. Flux retrievals

There exist several well-established algorithms for deriving point source emission fluxes from measurements of vertically integrated trace gas columns (Jacob et al., 2022; Theys et al., 2013). In the simplest case where the assumptions can be made of (i) a stationary emission flux, (ii) first order loss terms and (iii) a plume that is captured in full by the measurements, mass balance dictates (Seinfeld and Pandis, 2016):

$$Q = \frac{M}{\tau}, \tag{2}$$

with Q the emission flux, M the total plume mass (minus background) and τ the atmospheric lifetime of the species under consideration. The mass M should in this case be estimated from measurements within a sufficiently large box around the point source, so that transport out of the box can be neglected. As such, this method has been frequently applied to derive average emission fluxes from satellite measurements of short-lived species such as NO_2 (Beirle et al., 2011), SO_2 (McLinden

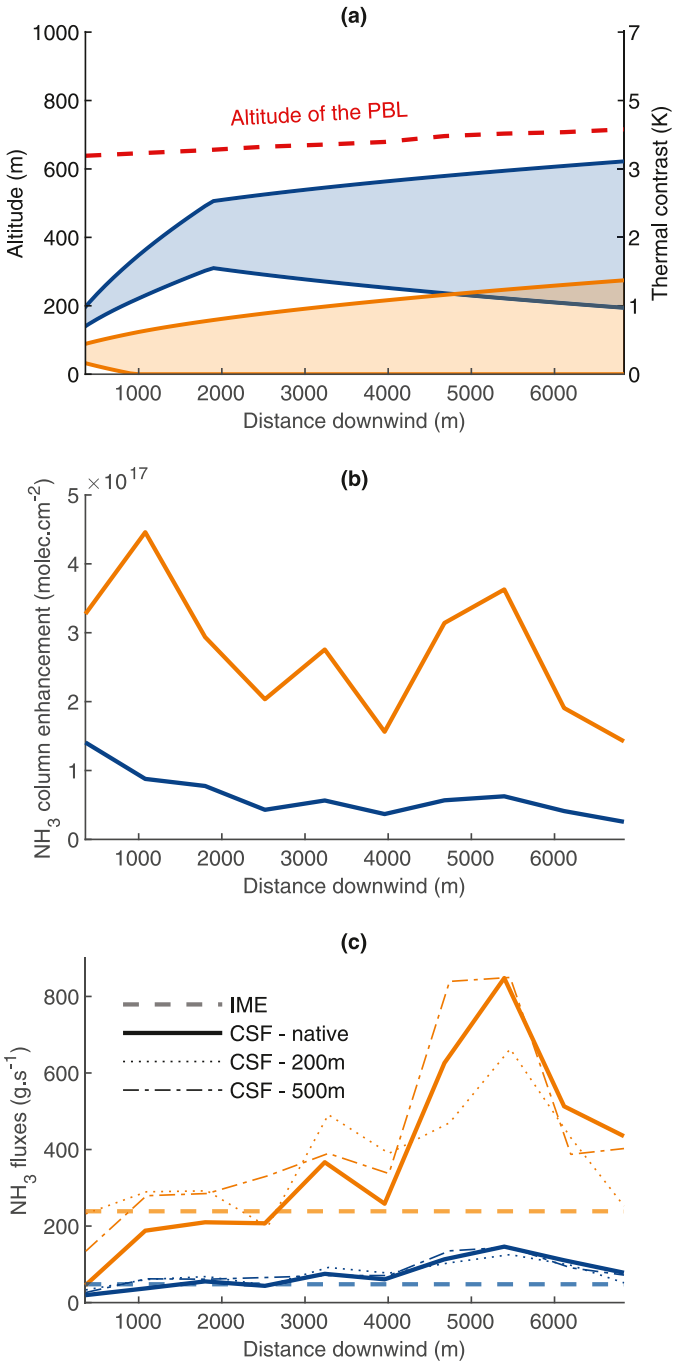

Fig. 5. (a) Two scenarios of plume rise and dispersion behaviour during transport downwind from the point source: non-rising (orange) and buoyant (blue). These two contrasting scenarios were modelled for a neutral atmosphere with an average wind speed of 7 m s^{-1} (see Appendix). The shaded areas represent $h \pm 2\sigma_z$. The values indicated on the right y-axis refer to the thermal contrasts between the surface and the parcel of air at the corresponding altitude indicated on the left axis. (b) NH_3 column enhancements with respect to the background, retrieved by inversion of the 10 spectra defined in Fig. 4. The two curves correspond to the two plume rise assumptions shown in the upper panel. (c) Fluxes calculated with the IME (dashed lines) and the CSF (solid lines) methods from native data. Emission rates retrieved with the CSF method from data degraded at spatial resolutions of 200 m (dotted lines) and of 500 m (dash–dotted lines). (For interpretation of the references to colour in this figure legend, the reader is referred to the web version of this article.)

et al., 2016), and NH_3 (Van Damme et al., 2018). Several extensions and generalizations of the method exist, taking into account e.g. non-stationary fluxes and transport out of the box (Duncan et al.,

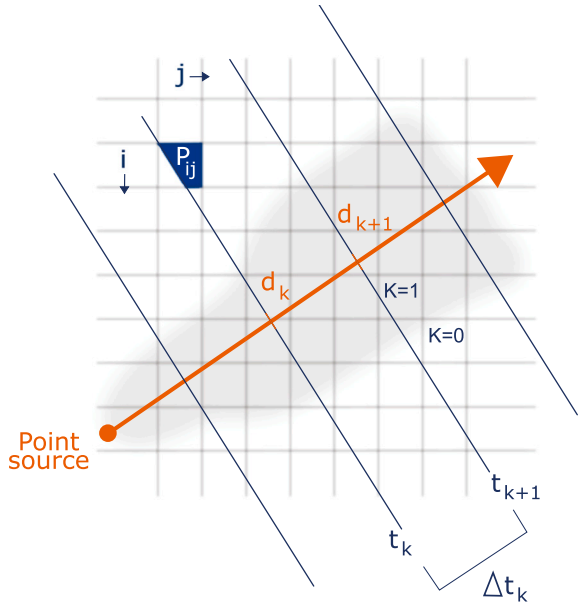

Fig. 6. Schematic illustration of the flux retrieval technique over a measurement grid. Traverses (blue) are perpendicular to the transport of the plume (orange) and spaced by a time-step Δt_k. The cell (i, j) is partially coloured in blue illustrating the overlap of this cell and the time-slice Δt_k defined by the traverses t_k and t_{k+1}. The plume mask K equals 1 inside the plume and 0 outside. (For interpretation of the references to colour in this figure legend, the reader is referred to the web version of this article.)

2013). Here, we apply two complementary techniques particularly well applicable on high resolution aircraft measurements of individual plumes.

The first one is the integrated mass enhancement (IME) method (Frankenberg et al., 2016; Varon et al., 2018). It is suited for longer-lived species or when the downwind plume is only captured partially (as with aircraft measurements). The main idea of the method is replacing the atmospheric lifetime τ with a residence lifetime τ_{res} that represents the average lifetime of the pollutant in the observed plume, thereby taking into account deposition, transport out of the observation box and turbulent diffusion:

$$Q_{IME} = \frac{M}{\tau_{res}} \tag{3}$$

Using large eddy simulations, Varon et al. (2018) found the following empirical relation for the residence lifetime:

$$\tau_{res} = L/(1.1 \log U + 0.6), \tag{4}$$

with U the horizontal ambient wind speed and L the square root of the surface area of the observed plume.

The cross-sectional flux (CSF) method (also known as the traverse method) is another extension of the basic mass balance method. It allows reconstructing the flux history of sources whose emissions vary rapidly over time (Theys et al., 2013; Varon et al., 2018). The method works by dividing the plume into k different sections delimited by planes perpendicular to the surface and to the main wind direction (see Fig. 6). Relying on knowledge of the wind speed U_k in each slice, distances d_k downwind can be converted back into time $t_k = \sum_{\tilde{k}=1}^{k-1} d_{\tilde{k}}/U_{\tilde{k}}$. Applying mass balance on a single slice between a distance d_k and d_{k+1} from the source, it is easy to see that the mean emission flux between a time $-t_{k+1}$ and $-t_k$ prior to the observation can be written as:

$$Q_{CSF}(-t_{k+1} \rightarrow -t_k) = \frac{M_k}{\Delta t_k} e^{t_k/\tau}, \tag{5}$$

with M_k the total mass in the slice k and $\Delta t_k = t_{k+1} - t_k$ the time it takes for the plume to travel a distance $\Delta d_k = d_{k+1} - d_k = \Delta t_k U_k$. The

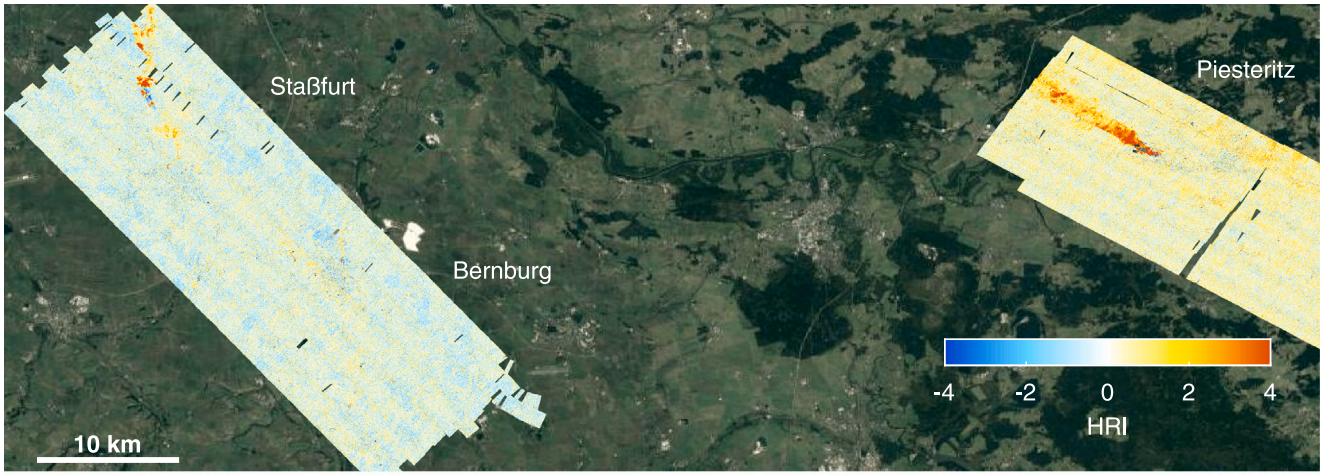

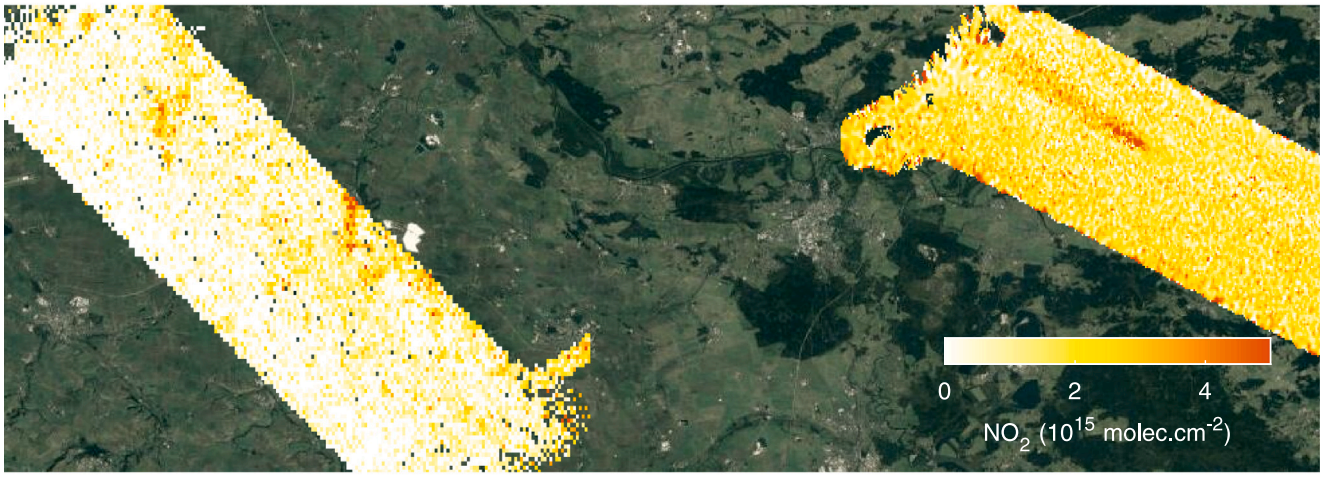

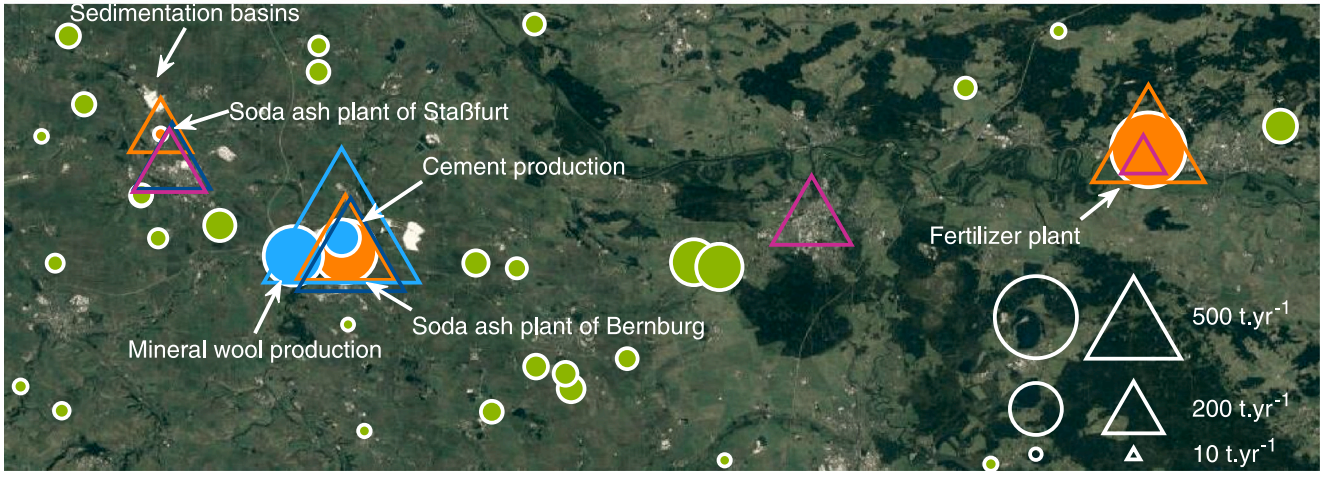

Chemical industry
Mineral industry
Intensive livestock production and aquaculture

Chemical industry
Mineral industry
Waste and waste water management
Energy sector

Fig. 7. The top panel shows the NH_3 HRI distributions at 12 m resolution; the middle panel shows NO_2 columns over Staßfurt and Bernburg (from measurements performed on 09/05/21) and over Piesteritz (from data measured on 28/04/21) and the bottom panel depicts the NH_3 (circles) and NO_2 (triangles) sources catalogued in the E-PRTR inventory between 2009 and 2015. The sizes of these circles/triangles are indicators of the flux magnitudes.

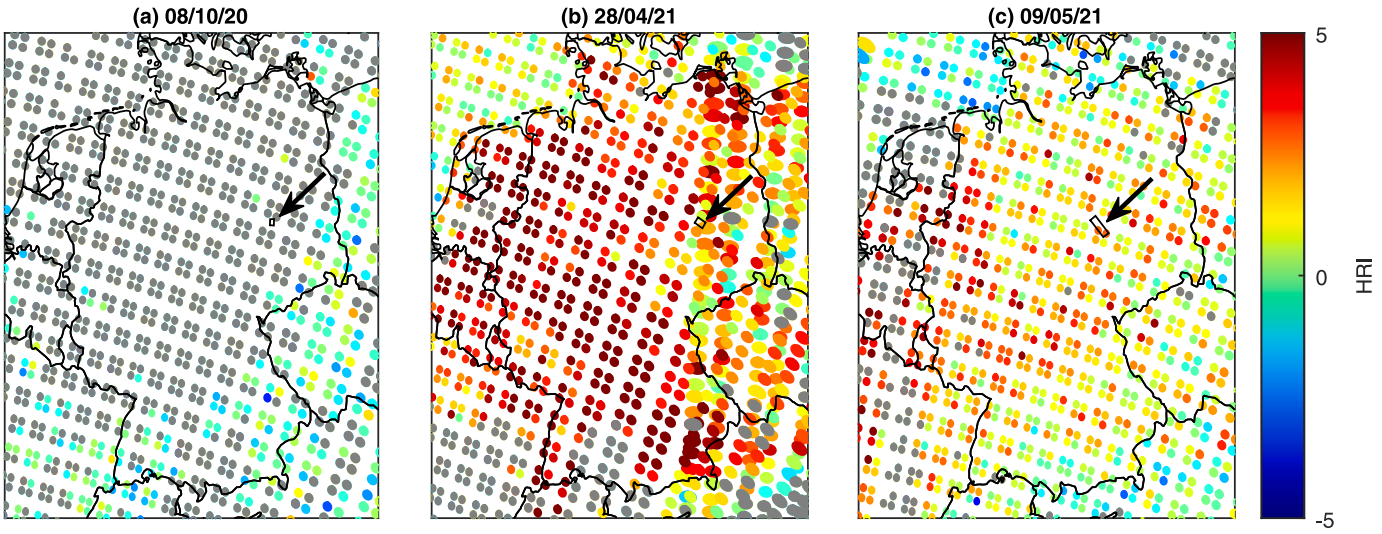

Fig. 8. NH_3 HRI distributions over Germany calculated from IASI measurements (on-board of Metop-B platform, from the morning overpass) whose pixel size and shape depend on the viewing angle of the instrument (Clerbaux et al., 2009). The different panels correspond to the data measured (a) on 08/10/20 (first flight over Piesteritz), (b) on 28/04/21 (second flight over Piesteritz) and (c) on 09/05/21 (flight over the Staßfurt/Bernburg area). The black rectangles correspond to the surveyed areas. Pixels in grey are contaminated with clouds.

factor $e^{t_k/\tau}$ corrects for deposition and chemical losses. Here we assume a lifetime of 2 h for NH_3.

Both methods are easily applicable on the NH_3 columns presented in the previous section. First, for each of the 10 transects of the plume, the total columns are multiplied by the respective surface area and converted to a slice mass. The IME method is then simply applied on the sum of all slice masses, using an average wind speed of 7 m s^{-1} estimated from ERA5 data. The application of the CSF method is equally straightforward using Eq. (5) and interpolated ERA5 wind speeds U_k. The results are detailed in Table 1 and shown on Fig. 5c with dashed (IME) and solid (CSF) lines. Both scenarios exhibit a decrease of fluxes over time (or an increase with distance) with the CSF method, but to a lesser extent in the higher altitude scenario. As we do not expect to observe a large variability of industrial emissions within 18 min (time taken for the plume to travel 7400 m downwind the source considering at an average wind speed of 7 m s^{-1}) this leads us to believe that there was at least some plume rise. It is also likely that the measurements have little or no sensitivity to the NH_3 located closest to the surface, with a thermal contrast barely above zero, resulting in an underestimation of the columns measured closest to the source. On the whole, we observe a good agreement between the IME and CSF flux estimates. The most plausible scenario (blue) provides a lower bound to the average flux of 60 g s^{-1} equivalent to 1900 t yr^{-1} if we consider constant emissions. According to the European Pollutant Release and Transfer Register (E-PRTR), atmospheric NH_3 emissions from this industrial complex amounts to 400 t yr^{-1} (European Environment Agency, 2021), which is considerably lower than our estimate.

The high spatial resolution of the Hyper-Cam LW instrument makes it straightforward to apply the CSF method, as observations are easily attributed to a single transect. However, a future Nitrosat would fly at a considerable coarser resolution, with footprints not necessarily aligned with the transects. Fortunately, the method can easily be adapted. Suppose we have an observation grid (i, j) as shown in Fig. 6, with retrieved cell masses M_{ij}. First a boolean plume mask K_{ij} is established which flags all cells that are assumed to be part of the plume. In our case, this is done by setting a threshold value of 2 on the HRI. Next and similar as before, a number of appropriate transects are introduced perpendicular to the wind direction. For a given time slice Δt_k the fractional overlap $P_{ij}(-t_{k+1} \rightarrow -t_k)$ is then calculated between each cell (i, j) and the transect k. With this, the mass M_k of the slice k can be written as

$$M_k = \sum_{ij} P_{ij}(-t_{k+1} \rightarrow -t_k) M_{ij} K_{ij} \tag{6}$$

and Eq. (5) can be applied as before. The resulting emission rates are shown in Fig. 5c with dotted and dash–dotted lines from data degraded at spatial resolutions of 200 and 500 m, respectively. The fluxes obtained in this way are fully consistent with the ones obtained before, showing the consistency of the approach and the potential of a future Nitrosat to provide robust constraints on individual point source emitters in a single overpass of the instrument.

3. NH_3 measured by Hyper-Cam LW in spring 2021

A second campaign took place in the spring of 2021, with a flight over Piesteritz on 28 April and a flight on 9 May over a large area that includes the cities Staßfurt and Bernburg. This second area was chosen as a target as it includes several different (industrial) sources of NO_2 and NH_3 according to the E-PRTR inventory (see bottom panel of Fig. 7).

Two instruments were on board the aircraft, which flew over the two areas at 3 km altitude: the Hyper-Cam LW, measuring NH_3 at a spatial resolution of 4 m and with a spectral sampling of 1.32 cm^{-1} and the SWING+ instrument, measuring NO_2 at a spatial resolution of 180 m.

As for the first campaign presented in the previous section, an HRI was setup for the detection of NH_3. Since both spring flights used the same spectral sampling, a common mean spectrum and associated covariance matrix could be calculated. The resulting distributions are presented in the top panel of Fig. 7, as before degraded to a spatial resolution of 12 m. Before analysing the distributions in more detail, we note that the HRI background levels are higher for the Piesteritz scene than for the Staßfurt/Bernburg area, indicating either higher background levels of NH_3 or higher thermal contrast. The HRI distributions measured by the satellite sounder IASI, shown in Fig. 8, confirm these results, and indicate that during both flights, enhanced levels of NH_3 were present over much of Germany. This background is likely related to fertilization of fields, which leads to a yearly peak in the NH_3 concentrations in spring over Europe (Paulot et al., 2014).

3.1. Piesteritz

Just as in the first campaign, we observe a large plume coming from the Piesteritz industrial complex, this time transported in northwest direction. While there are some other small local enhancements

Table 1
The first part of the table lists the mean atmospheric conditions at the level of the detected NH_3 plumes, for the two flights over Piesteritz (autumn 2020 and spring 2021). The second part of the table shows the range of emission fluxes of NH_3 from the fertilizer plant in Piesteritz retrieved with distinct approaches for the buoyant/non-rising plume.

Variable	Autumn 2020	Spring 2021
Overpass time (local time)	10.20 AM–10.40 AM	11.40 AM–11.50 AM
NH_3 background	2.9 10^{15} molec cm^{-2}	3.7 10^{15} molec cm^{-2}
Average surface temperature T_s	285 K	290 K
Average wind speed U	6.8 m s^{-1}	4.0 m s^{-1}
Average PBL height	640–720 m	1070–1210 m
Average thermal contrast (at the surface/PBL)	0/4 K	3/12 K
Stability class (see Appendix A.3)	Neutral (D)	Slightly unstable (C)
Flux retrieval method	**Autumn 2020**	**Spring 2021**
IME	1600/7600 t yr^{-1}	1600/3200 t yr^{-1}
CSF - native	2200/12 000 t yr^{-1}	2200/4400 t yr^{-1}
CSF - 200 m	2200/12 000 t yr^{-1}	2500/5400 t yr^{-1}
CSF - 500 m	2500/13 000 t yr^{-1}	2500/5400 t yr^{-1}

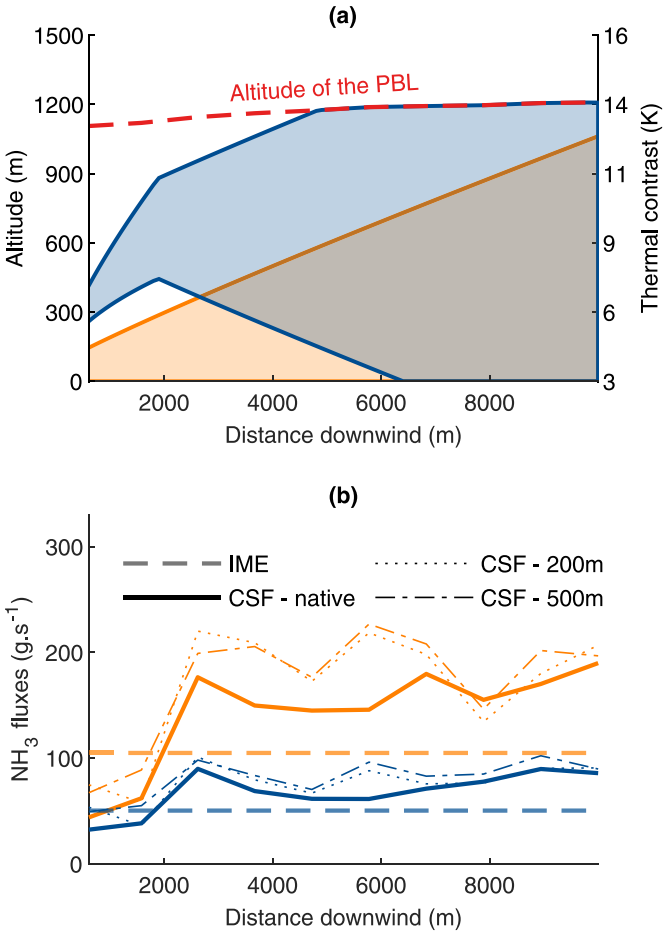

Fig. 9. Top panel: same as Fig. 5a (but for a slightly unstable atmosphere with an average wind speed of 4 m s^{-1}). Bottom panel: same as Fig. 5c for the Piesteritz survey of 28 April 2021.

on the map, none of them could be attributed with a good degree of confidence to a specific source. We derived NH_3 fluxes using the same procedure as before, with again two different assumed vertical dispersion models (see Fig. 9a and Appendix). Note that these profiles exhibit a larger vertical dispersion compared to the one in autumn-time, consistent with the more unstable atmospheric conditions. The measurement conditions were excellent, with positive thermal contrast for the entire boundary layer, extending up to 13 K at the top. Using the IME and the CSF methods, the emission rates were estimated between 50 and 140 g s^{-1} (equivalent to 1600 and 4400 t yr^{-1} for constant emissions). The fluxes were also computed from the data degraded at 200 and 500 m resolutions, with similar results (Fig. 9b).

As summarized in Table 1, the lower bounds on the derived fluxes are in good agreement, again indicating that the scenario of a buoyant plume, is the most likely one. The fluxes calculated with the IME method are lower than those calculated with the CSF technique because a longer lifetime is considered. Indeed, the residence lifetime defined by Eq. (4) takes into account the diffusion of NH_3 in all directions while the CSF technique considers that transport occurs in a straight line. We also note that the relative difference between the fluxes calculated for the two scenarios is significantly smaller for the second (factor 2) than the first flight (factor 5), probably because of the better thermal contrast. This demonstrates that when the measurement conditions (thermal contrast) are better, the retrievals depend less on plume altitude assumptions.

As the SWING+ instrument was operational for this campaign we could also analyse its measurements. The instrument (Merlaud et al., 2018, 2020; Tack et al., 2019) is a compact whiskbroom imager dedicated to mapping NO_2 and SO_2 with the DOAS (Differential Optical Absorption Spectroscopy) technique (Platt and Stutz, 2008). SWING+ uses a UV–Vis spectrometer (Avantes ULS2048X64-EVO), an arduino-controlled scanner, a 7 × 100 μm bundle-slit fibre, and a PC. It records spectra between 280 and 550 nm at a spectral resolution of 0.8 nm FWHM (Full Width at Half Maximum). The typical sampling frequency is 2 Hz and the spatial resolution at 3 km altitude is 180 m. We analysed the spectra with the QDOAS software (Fayt et al., 2011), which retrieves the differential slant column densities (SCDs) of NO_2 for each spectra relative to a reference spectrum of the same flight. The reference spectrum is an average of 25 spectra recorded over a clean area. The SCDs are converted to vertical column densities (VCDs) applying an air mass factor (AMF). NO_2 box AMFs have been calculated with the LIDORT 2.6 radiative transfer model (RTM) (Spurr, 2008), and we assumed a NO_2 residual amount in the reference spectrum of 1.0 10^{15} molec cm^{-2}.

The SWING+ data allowed to highlight a co-located plume of NO_2 emitted by the industry (see middle panel of Fig. 7). This represents the first simultaneous measurement of the two main Nr compounds from remote sensing. The observed NO_2 is probably linked to the large-scale production of nitric acid (HNO_3) at the Piesteritz plant. Production of HNO_3 starts with oxidation of NH_3 to form NO_x (nitric oxide (NO) and NO_2), which then after absorption in water forms HNO_3. In the entire process, substantial quantities of NO_2 are emitted to air (European Commission, 2007; European Environment Agency, 2019). NO_2 emissions originating from the factory were estimated with the CSF method adapted for coarser resolutions described earlier and amount to 200 t yr^{-1}, assuming constant fluxes. This value is then multiplied by a factor 1.32 to take into account the NO_x/NO_2 partitioning (Shaiganfar et al., 2011) and yields to NO_x emissions of 260 t yr^{-1}, which are significantly lower than the 700 t yr^{-1} reported in the E-PRTR database.

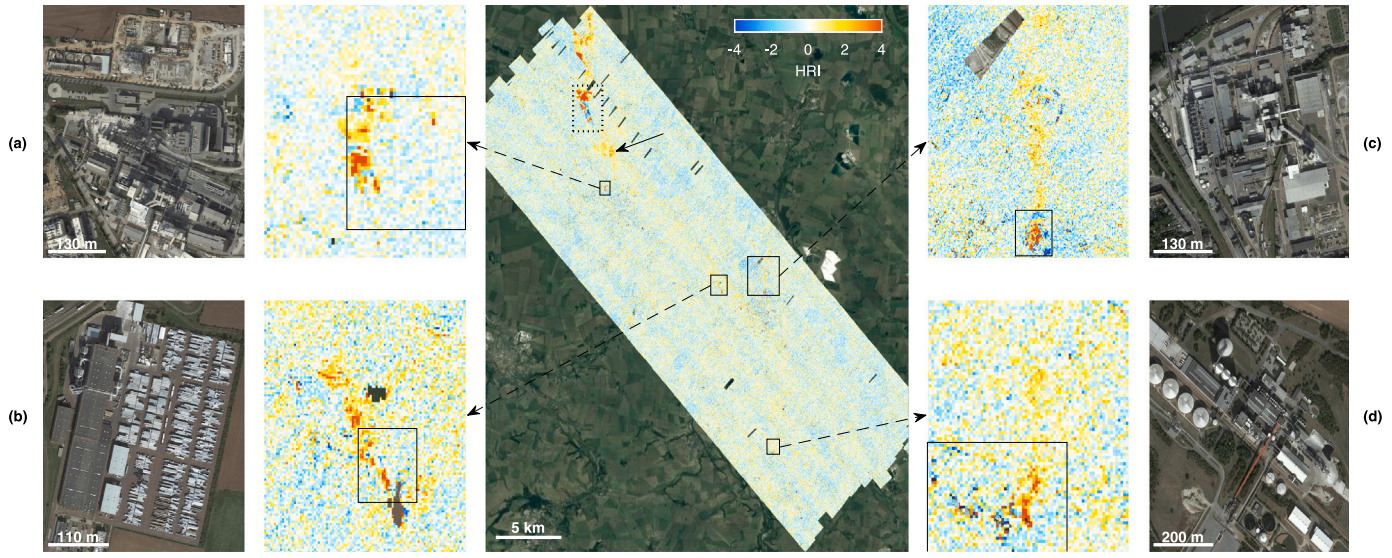

Fig. 10. The central panel depicts the NH_3 HRI distribution at 12 m resolution over the Staßfurt/Bernburg (Germany) area (displayed on Fig. 7) superimposed on satellite visible imagery from Google Maps. The side panels provide close-up views on point sources detected over this area: (a) the soda ash plant of Staßfurt, (b) the wool production factory, (c) the Bernburg industry producing soda ash and (d) the sugar factory. The dotted box corresponds to the zone shown in Fig. 11.

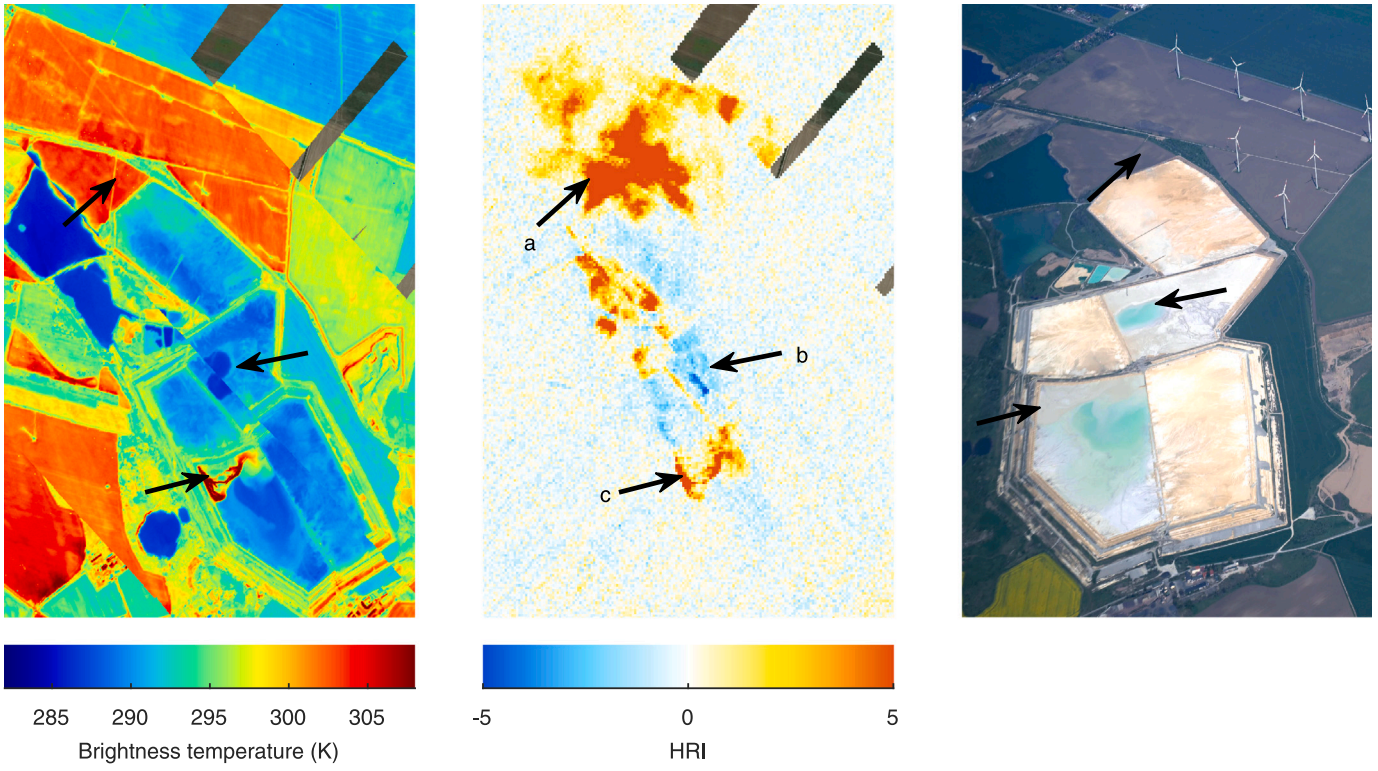

Fig. 11. Close-up views over the settling ponds delimited by the dotted box in Fig. 10. From left to right, they show the brightness temperature distribution, the HRI distribution at 12 m resolution and a picture of the basins taken during the flight. The letters a, b and c point respectively to a transported plume, a cold part of the basin and a very hot part of the basin. They refer to the panels (a), (b) and (c) of Fig. 12.

3.2. Staßfurt and Bernburg

In this section, we present a qualitative analysis of the measurements over the Staßfurt/Bernburg area, which took place on Sunday 9 May 2021. Turbulent air made flying at a constant altitude and speed difficult, and this likely affected the measured spectra. It could be the reason why the agricultural sites included in the E-PRTR as NH_3 emitters and mapped in the bottom panel of Fig. 7 (green) were not seen. Nonetheless, combining analyses of the HRI distribution, together with the satellite visible imagery and the E-PRTR register led to several discoveries, which are illustrated on Fig. 10 and discussed below.

A clear plume is seen near a factory that produces mineral wool insulation (Fig. 10b). Production of such insulation is a known source of NH_3 (Battye et al., 1994), where it is used as a pH-regulator. Almost all of the NH_3 is released and emitted into the atmosphere at the end of the production process (Kowatsch, 2010). A small NH_3 plume is seen near a sugar industry south of Bernburg (Fig. 10d). Even though sugar factories are known to emit NH_3 (Chen et al., 2022), this site is not included

in the E-PRTR inventory (bottom panel of Fig. 7). In order to confirm the validity of the HRIs, we applied a spectral whitening technique that allows exposing spectral enhancements (see De Longueville et al. (2021) for more information). The results, shown in Fig. 12, confirm irrefutably the validity of the NH_3 HRI enhancements highlighted in Fig. 10.

Small NH_3 plumes are observed directly over the chemical plants producing soda ash (Na_2CO_3) in Staßfurt (illustrated on panel (a)) and Bernburg (panel (c)). Within the Solvay process that is used to synthesize soda ash, NH_3 is a catalyst and is continuously recovered and reused. Yet, some emissions to air are unavoidable (Ecofys et al., 2009) as confirmed by our measurements. Just north of the Staßfurt plume there are several detections of NH_3 (indicated with an arrow in the central panel of Fig. 10), which could be transported NH_3 downwind from the Staßfurt plant, as no other nearby source was identified. The emissions from both soda ash plants are reported in the E-PRTR inventory amounting on average to 14 t yr^{-1} for the Staßfurt plant and 300 t yr^{-1} for Bernburg.

North of Staßfurt there is a large plume which seemingly originates from the large sedimentation basins associated with the soda ash plant, as shown in Fig. 11. The synthesis of soda ash produces wastewater with a very high fraction of suspended solids, that cannot be discharged as such. For this reason, settling ponds are operated to decant these solids. Several basins are used in parallel, with one basin receiving new effluents, while others are left to drain and dry completely (Federal Environmental Agency, 2001; European Commission, 2007; IL & FS Ecosmart Limited, 2010). Fig. 11 shows the measured brightness temperatures, the NH_3 HRIs and a photograph of the basins taken from the aircraft at the time of the flight. The temperature plot on the left reveals the precise location where new effluents are discharged, reaching temperatures over 320 K. It is also the place where the largest NH_3 HRIs are observed (up to 58). Large HRIs up to 29 are also found over the high-temperature bare soils downwind of the basins. In contrast, negative HRIs down to −7 are found over the other (colder) basins. No elevated HRIs are observed over the rightmost basin. Fig. 12 shows the whitened spectra (a) in the transported plume, (b) over a cold part of the basin and (c) over the very hot part of the basin. In all three cases again confirming the NH_3 detections.

These observations strongly suggest that the NH_3 plume originates from the warm fresh effluents. Its transport downwind north shows up in the HRI imagery either as NH_3 in emission or absorption depending on the underlying surface temperature. Given the fact that wastewater from soda ash production contains elevated quantities of dissolved ammonium (European Commission, 2007), it is not surprising that a significant amount is directly volatilized upon discharge. The elevated temperature and alkaline pH (Federal Environmental Agency, 2001; Steinhauser, 2008) of the effluent likely play a role, as these are two characteristics that highly favour volatilization of NH_3 (Cai, 1997; Freney et al., 1983).

As mentioned before, chimney stack exhausts, associated with soda ash production, are well-known to be a source of NH_3 emissions in the air (European Commission, 2007). However, to our knowledge it is the first time that NH_3 emissions are reported from a soda ash settling pond. As the HRI distributions suggest, the latter could be the dominant source of emissions from certain soda ash plants. Note that the sedimentation basins of the Bernburg soda ash plant were unfortunately not within the surveyed area, so that no conclusions can be drawn on whether such emissions also occur at sedimentation basins of that plant.

Among the various NH_3 plumes, only the largest one from Staßfurt can clearly be detected from the downsampled data at a resolution of 500 m, similar to what Nitrosat would observe (see Fig. 13b). The other plumes are mostly smaller than 500 m and once averaged over the entire pixel do not stand out from the background, highlighting the importance of the signal-to-noise ratio in the design of a future Nitrosat sounder. The 2000 m average (panel (c)) highlights a dramatic

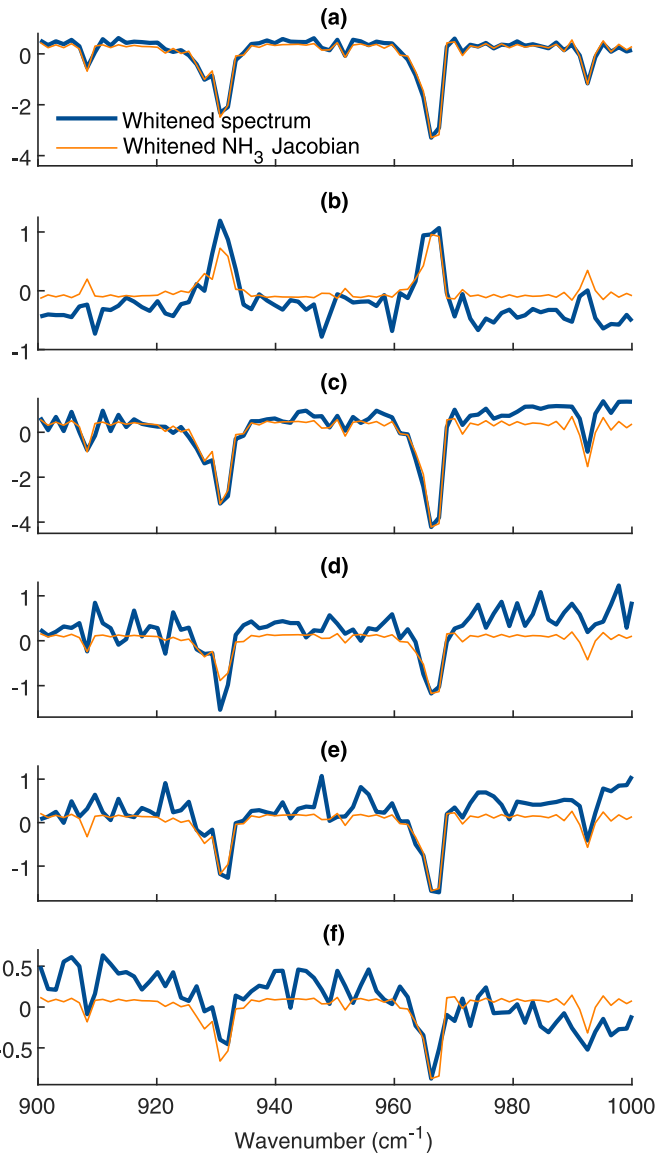

Fig. 12. Whitened spectra over the identified hotspots. The spectra in panels (a), (b) and (c) correspond to average spectra from the areas a, b and c marked by arrows in Fig. 11. The bottom panels illustrate whitened spectra over (d) the sugar factory (d in Fig. 10), (e) the soda ash plant of Bernburg (c in Fig. 10) and (f) the wool production factory (b in Fig. 10). They all exhibit NH_3 signals, corroborated by the whitened NH_3 Jacobian (orange). (For interpretation of the references to colour in this figure legend, the reader is referred to the web version of this article.)

consequence of averaging, with an HRI over the sedimentation pond close to 0. In this case emission and absorption by NH_3 cancel each other completely, and retrievals over such a pixel would result in columns with a very large uncertainty (as both the HRI and thermal contrast are close to zero).

4. Discussion and conclusion

Airborne hyperspectral infrared observations of atmospheric NH_3 emissions have been reported before. Hulley et al. (2016) detected, among other species, NH_3 over a refinery and natural gas-fired power plant site in California with the Hyperspectral Thermal Emission Spectrometer (HyTES). The same instrument was used by Kuai et al. (2019) to detect and quantify NH_3 over a smouldering fire, a power plant and a large feedlot. Tratt et al. (2011, 2013) reported NH_3 measurements

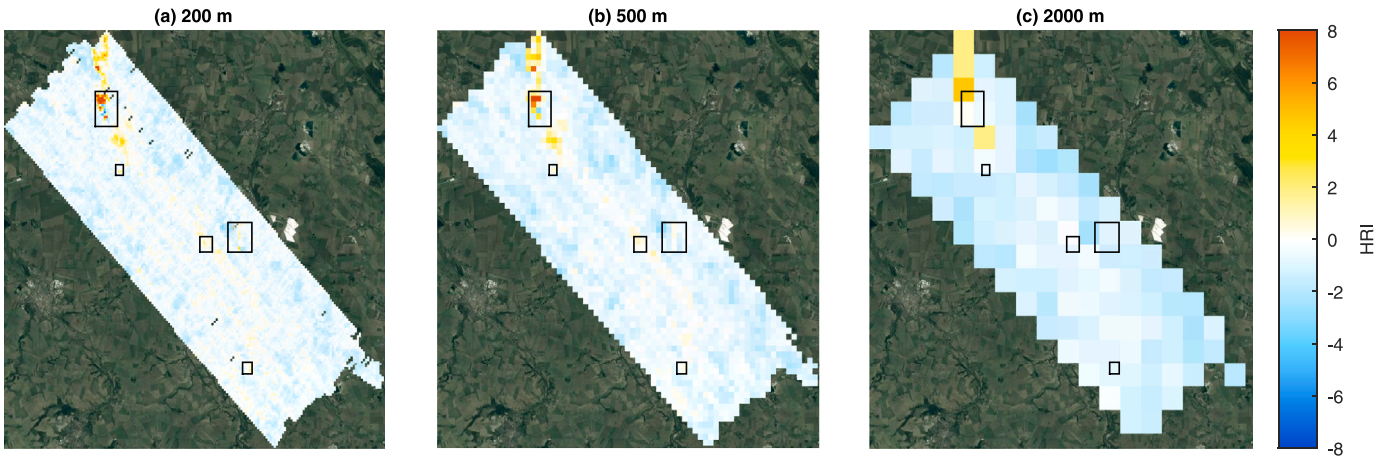

Fig. 13. NH_3 HRI distributions from the Staßfurt/Bernburg area downsampled at spatial resolutions of (a) 200 m, (b) 500 m and (c) 2000 m. The black boxes refer to the zones discussed in Fig. 10.

of fumarolic vents and from sea-bird colonies in California. They also calculated NH_3 flow rates from the geothermal fumaroles field using a mass balance approach (Tratt et al., 2016). With this paper, we add to this list of observations, a production facility of synthetic NH_3, two soda ash plants, a mineral wool insulation factory and a sugar factory, as well as simultaneous observations of NH_3 and NO_2 plumes.

The observations over the fertilizer plant presented here, are particularly important as such plants are the single largest point source emitters of NH_3. Worldwide, over 250 such ultra-emitters have been identified using the existing landscape of satellite sounders (Clarisse et al., 2019b). However, these mostly concern isolated plants, and many plants located in industrial clusters or nearby other large sources remain unidentified due to the coarse spatial resolution (>10 km) of current satellite sounders. In addition, with large spatial gaps between adjacent observations, none of the current sounders offers imaging capability. Because of these limitations, long-term temporal averages are required for the identification of sources and derivation of emission fluxes. Furthermore, current spaceborne emission estimates come with very large uncertainties related to the difficulty in estimating background columns and the propagation of the uncertain knowledge of the atmospheric lifetime of NH_3 (Dammers et al., 2019; Van Damme et al., 2018).

As we have shown in this paper, most of these problems would be overcome with a satellite hyperspectral imager like Nitrosat, that offers a spatial resolution below 500 m. This resolution would be sufficient to observe, in a single overpass, an entire NH_3 plume emanating from an individual point source emitter. The background levels of NH_3 are in such measurements straightforwardly estimated, and because the plume can be observed at very short distances downwind, the lifetime problem is practically non-existent. We have demonstrated the consistency of the IME and CSF methods to derive emissions, using the native measurements and using simulated observational pixels of 200 and 500 m.

The remaining largest source of uncertainty of the emissions is the vertical profile of NH_3. Assumptions on the profile are required to take into account the dependence of the strength of the NH_3 spectral signal on the magnitude of the thermal contrast. In previous studies, vertical column densities were retrieved using fixed vertical profile assumptions. In this study, we have for the first time used dynamic vertical profiles, that vary with the distance downwind. Using two contrasting scenarios for plume rise we have shown that the retrieved emission fluxes can vary greatly. Fortunately, for larger thermal contrasts, as we saw with the spring-time flight over Piesteritz, the sensitivity to the assumptions becomes smaller. Furthermore, the differences between different plume rise scenarios are smaller very close or for distances far downwind the source, as can be seen from Fig. 9a. In the former case, plumes are still close to the chimney height, while in the latter case plumes become increasingly well-mixed throughout the vertical extent of the boundary layer. A future Nitrosat, with a foreseen swath of 80 km, will capture plumes much further downwind, and exploiting its high spatial resolution, emission estimates could be based on the part of the plume furthest downwind. Another idea that could be explored is to retrieve altitude information directly from the measurements by assuming steady-state emissions, i.e. what vertical plume rise assumption would yield a constant emission flux?

While Nitrosat targets both NO_2 and NH_3, the focus of this paper has been on NH_3 measurements as several other demonstration campaigns previously highlighted the advantage of high spatial resolution measurement for NO_2 source identification and quantification (Fujinawa et al., 2021; Meier et al., 2017; Souri et al., 2018). As an example, the measurements presented in Tack et al. (2021) convincingly demonstrate that a spatial resolution of less than 1 km is required to identify and separate individual point sources in the industrial cluster of Antwerp harbour (Belgium). In the present study however, we showed the first example of large simultaneous emissions of NO_2 and NH_3.

The campaign over the Staßfurt/Bernburg area proved to be very interesting with the discovery of the large NH_3 emissions fluxes from the sedimentation basins of the soda ash plant in Staßfurt. Several other and smaller industrial plumes were seen as well, similar in size as the ones previously seen by HyTES. Such smaller plumes only cover one or two measurement pixels of a future Nitrosat. However, nothing would prevent also in this case to estimate emission fluxes using e.g. the IME method. Attributing the precise source of these to specific industrial processes would also be straightforward in regions where industries are well spread out. However, in larger industrial clusters, with many potential emitters, identification of smaller sources would prove more challenging and would require temporal averaging or the use of third party information on the type of activities carried out.

Using HyTES, Kuai et al. (2019) were able to capture large NH_3 plumes directly over the feedlots in the U.S. However, transport over longer distance (>500 m) was not reported, nor was the derivation of emission fluxes. What is currently missing in terms of Nitrosat demonstration, is comprehensive and representative survey flights over agricultural areas, together with a demonstration that agricultural emission fluxes can be retrieved in a complex landscape of smaller sources. For this reason, in the summer of 2022 several flights took place over the Po Valley in Italy, the largest NH_3 hotspot region in Europe and home to many small and large farms. The analysis of the results of the campaign are underway and will be subject of a follow-up study.

CRediT authorship contribution statement

Lara Noppen: Conceptualization, Writing – original draft, Analysis, The column and flux retrievals, Prepared the figures, Campaign planning, Revision of the manuscript, Interpretation of the results. **Lieven Clarisse:** Conceptualization, Writing – original draft, Campaign planning, Revision of the manuscript, Interpretation of the results. **Frederik Tack:** Responsible for the NO_2 measurements, Campaign planning, Revision of the manuscript, Interpretation of the results. **Thomas Ruhtz:** Organized the campaigns, Carried out the measurements, Campaign planning, Revision of the manuscript, Interpretation of the results. **Alexis Merlaud:** Responsible for the NO_2 measurements, Campaign planning, Revision of the manuscript, Interpretation of the results. **Martin Van Damme:** Campaign planning, Revision of the manuscript, Interpretation of the results. **Michel Van Roozendael:** Responsible for the NO_2 measurements, Campaign planning, Revision of the manuscript, Interpretation of the results. **Dirk Schuettemeyer:** Campaign planning, Revision of the manuscript, Interpretation of the results. **Pierre Coheur:** Campaign planning, Revision of the manuscript, Interpretation of the results.

Declaration of competing interest

The authors declare that they have no known competing financial interests or personal relationships that could have appeared to influence the work reported in this paper.

Data availability

The data that has been used is confidential

Acknowledgements

The authors gratefully acknowledge the European Space Agency (ESA) for funding the Nitrocam campaigns. The authors also gratefully acknowledge GFZ and FUB for the use of the Telops instrument and for their support and cooperation during the campaign. The research was co-funded by the Belgian State Federal Office for Scientific, Technical and Cultural Affairs (Prodex HIRS) and the Air Liquide Foundation (TAPIR project). This work is also partly supported by the FED-tWIN project ARENBERG ("Assessing the Reactive Nitrogen Budget and Emissions at Regional and Global Scales") funded via the Belgian Science Policy Office (BELSPO). L. Clarisse is Research Associate supported by the Belgian F.R.S.-FNRS. This publication is supported by the French Community of Belgium in the framework of a FRIA grant. The authors thank D. Jacob for discussions about plume dispersion.

Appendix. Plume dispersion model

A.1. The Gaussian plume model

Assuming homogeneous steady-state winds and a steady-state point source, plume behaviour can be described with a Gaussian plume dispersion model, which as a formal solution to the advection–diffusion equation, takes into account both advection and atmospheric diffusion (Stockie, 2011). Neglecting the reflection from the ground and from the planetary boundary layer (PBL), the solution can be written as:

$$C(x,y,z) = \frac{Q}{2\pi\sigma_y\sigma_z U} e^{\frac{-y^2}{2\sigma_y^2}} e^{-\frac{(z-h)^2}{2\sigma_z^2}}, \tag{7}$$

where $C(x,y,z)$ is the concentration at the position specified by the downwind (x), crosswind (y) and vertical (z) directions, Q the source flux rate, U the horizontal wind speed and $h(x)$ the central height h of the plume as a function of its distance downwind from the source x. The standard deviations $\sigma_y(x)$ and $\sigma_z(x)$ describe the horizontal and vertical spreads of the plume along the y and z axis. In case of vertical integrated measurements, all that matters is the shape of the vertical profile. For our retrieval, we can therefore use the following reduced form of Eq. (7):

$$C(x,z) = C_{\text{peak}} e^{-\frac{(z-h)^2}{2\sigma_z^2}}, \tag{8}$$

with C_{peak} the a priori peak concentration. This equation has two unknowns, the central plume height h, and the vertical spread σ_z, which we now parametrize.

A.2. Advection and initial plume rise

At least initially, a plume often undergoes vertical transport, as a result of either its initial momentum, or its buoyancy, in case the emitted gas is hotter or less dense than the surrounding air. A common model for the central height h of a plume as a function of its distance downwind from the source x, the horizontal wind speed U and the initial buoyancy flux F is (De Visscher, 2014; Hanna et al., 1982):

$$h(x) = h_0 + \frac{1.6\, F^{\frac{1}{3}} x^{\frac{2}{3}}}{U}, \tag{9}$$

with h_0 the initial height at the source. This relationship is known as the '2/3 law' and is in agreement with the majority of field and laboratory data. The coefficient 1.6 is considered accurate within a range of ±40% whose variations are due to down-wash or local ground effects (Hanna et al., 1982). It is for example assumed to be 2 by Briggs (1965).

The buoyancy flux F depends on several factors such as the density, temperature and initial efflux velocity of the gas at the chimney and the radius of the stack, all of which we do not know. One scenario that we can exclude is that of very hot plumes, which would result in negative thermal contrast and negative HRIs. As these were not observed in any of the industrial plumes, we conclude that the initial buoyancy must be driven by its initial momentum and/or differences in density. For the study cases presented in Sections 2 and 3.1, we assumed both a small and a large value for F (5 and 1000 $m^4\ s^{-3}$).

However, plumes do not rise indefinitely but reach a maximum altitude referred to as the final plume rise height (Willis and Deardorff, 1983). This altitude is reached at a distance x_f downwind from the source that approximately satisfies (De Visscher, 2014):

$$\begin{aligned} x_f &= 49F^{\frac{5}{8}} \quad \text{for} \quad F < 55\ m^4\ s^{-3} \\ x_f &= 119F^{\frac{2}{5}} \quad \text{for} \quad F > 55\ m^4\ s^{-3} \end{aligned} \tag{10}$$

At distances greater than x_f, the altitude of the plume remains constant.

A.3. Diffusion

Plumes undergo vertical and horizontal mixing due to atmospheric turbulence, generated by buoyant air parcels and wind shear (Gulliver, 2012; Willis and Deardorff, 1983). The amount of diffusion varies greatly depending on the atmospheric conditions. The Pasquill–Gifford classification describes and classifies the stability of the boundary layer in six classes based on the surface wind speed, the sun insulation and the cloud cover (Gifford, 1961; Pasquill, 1961). The classes are: very unstable (A), unstable (B), slightly unstable (C), neutral (D), slightly stable (E) and stable (F).

In the Gaussian plume model, diffusion is characterized by the horizontal and vertical spread σ_y and σ_z. Here, we follow Martin (1976), who parametrized these in terms of stability classes as:

$$\sigma_y(x) = ax^b \quad \text{and} \quad \sigma_z(x) = cx^d + f, \tag{11}$$

where a, b, c, d and f are constants defined for each stability class.

For the study cases presented in Sections 2 and 3.1, the atmospheres can be considered, respectively, as neutral (D) and slightly unstable (C) according to the wind speed from ERA5 data and the sun insulation.

References

Aneja, V.P., Roelle, P.A., Murray, G.C., Southerland, J., Erisman, J.W., Fowler, D., Asman, W.A.H., Patni, N., 2001. Atmospheric nitrogen compounds II: emissions, transport, transformation, deposition and assessment. Atmos. Environ. 35 (11), 1903–1911.

Barret, B., Hurtmans, D., Carleer, M.R., De Mazière, M., Mahieu, E., Coheur, P.-F., 2005. Line narrowing effect on the retrieval of HF and HCl vertical profiles from ground-based FTIR measurements. J. Quant. Spectrosc. Radiat. Transfer 95 (4), 499–519.

Battye, R., Battye, W., Overcash, C., Fudge, S., 1994. Development and Selection of Ammonia Emission Factors. Technical Report, U.S. Environmental Protection Agency.

Bauduin, S., Clarisse, L., Theunissen, M., George, M., Hurtmans, D., Clerbaux, C., Coheur, P.-F., 2017. IASI's sensitivity to near-surface carbon monoxide (CO) theoretical analyses and retrievals on test cases. J. Quant. Spectrosc. Radiat. Transfer 189, 428–440.

Behera, S.N., Sharma, M., Aneja, V.P., Balasubramanian, R., 2013. Ammonia in the atmosphere: A review on emission sources, atmospheric chemistry and deposition on terrestrial bodies. Environ. Sci. Pollut. Res. 20 (11), 8092–8131.

Beirle, S., Boersma, K.F., Platt, U., Lawrence, M.G., Wagner, T., 2011. Megacity emissions and lifetimes of nitrogen oxides probed from space. Science 333 (6050), 1737–1739.

Bouwman, A.F., Lee, D.S., Asman, W.A.H., Dentener, F.J., Hoek, K.W.V.D., Olivier, J.G.J., 1997. A global high-resolution emission inventory for ammonia. Glob. Biogeochem. Cycles 11 (4), 561–587.

Bray, C.D., Battye, W., Aneja, V.P., Tong, D.Q., Lee, P., Tang, Y., 2018. Ammonia emissions from biomass burning in the continental United States. Atmos. Environ. 187, 50–61.

Briggs, G.A., 1965. A plume rise model compared with observations. J. Air Pollut. Control Assoc. 15 (9), 433–438.

Cai, G.-X., 1997. Ammonia volatilization. In: Zhu, Z.-l., Wen, Q.-x., Freney, J.R. (Eds.), Nitrogen in Soils of China. Springer Netherlands, Dordrecht, pp. 193–213.

Chen, Y., Shen, H., Kaiser, J., Hu, Y., Capps, S.L., Zhao, S., Hakami, A., Shih, J.-S., Pavur, G.K., Turner, M.D., Henze, D.K., Resler, J., Nenes, A., Napelenok, S.L., Bash, J.O., Fahey, K.M., Carmichael, G.R., Chai, T., Clarisse, L., Coheur, P.-F., Van Damme, M., Russell, A.G., 2021. High-resolution hybrid inversion of IASI ammonia columns to constrain US ammonia emissions using the CMAQ adjoint model. Atmos. Chem. Phys. 21 (3), 2067–2082.

Chen, Y., Zhang, Q., Cai, X., Zhang, H., Lin, H., Zheng, C., Guo, Z., Hu, S., Chen, L., Tao, S., Liu, M., Wang, X., 2022. Rapid increase in China's industrial ammonia emissions: Evidence from unit-based mapping. Environ. Sci. Technol..

Clarisse, L., Clerbaux, C., Franco, B., Hadji-Lazaro, J., Whitburn, S., Kopp, A.K., Hurtmans, D., Coheur, P.-F., 2019a. A decadal data set of global atmospheric dust retrieved from IASI satellite measurements. J. Geophys. Res.: Atmos. 124 (3), 1618–1647.

Clarisse, L., Shephard, M.W., Dentener, F., Hurtmans, D., Cady-Pereira, K., Karagulian, F., Van Damme, M., Clerbaux, C., Coheur, P.-F., 2010. Satellite monitoring of ammonia: A case study of the San Joaquin Valley. J. Geophys. Res. 115 (D13).

Clarisse, L., Tack, F., Ruhtz, T., Merlaud, A., Noppen, L., Van Damme, M., Schuettemeyer, D., Coheur, P., Van Roozendael, M., 2021. Aircraft observations of NO_2 and NH_3 over selected locations in Germany. In: EGU General Assembly 2021, EGU21-12645. p. 1.

Clarisse, L., Van Damme, M., Clerbaux, C., Coheur, P.-F., 2019b. Tracking down global NH_3 point sources with wind-adjusted superresolution. Atmos. Meas. Tech. 12 (10), 5457–5473.

Clerbaux, C., Boynard, A., Clarisse, L., George, M., Hadji-Lazaro, J., Herbin, H., Hurtmans, D., Pommier, M., Razavi, A., Turquety, S., Wespes, C., Coheur, P.-F., 2009. Monitoring of atmospheric composition using the thermal infrared IASI/MetOp sounder. Atmos. Chem. Phys. 9 (16), 6041–6054.

Coheur, P.-F., Levelt, P., Clarisse, L., Van Damme, M., Eskes, H., Veefkind, P., Clerbaux, C., Dentener, F., Erisman, J.W., Schaap, M., Sutton, M.A., Van Roozendael, M, 2021. Nitrosat, a satellite mission concept for mapping reactive nitrogen at the landscape scale. In: EGU General Assembly 2021, EGU21-9932. p. 1.

Dammers, E., McLinden, C.A., Griffin, D., Shephard, M.W., van der Graaf, S., Lutsch, E., Schaap, M., Gainairu-Matz, Y., Fioletov, V., Van Damme, M., Whitburn, S., Clarisse, L., Cady-Pereira, K., Clerbaux, C., Coheur, P.F., Erisman, J.W., 2019. NH_3 emissions from large point sources derived from CrIS and IASI satellite observations. Atmos. Chem. Phys. 19 (19), 12261–12293.

De Longueville, H., Clarisse, L., Whitburn, S., Franco, B., Bauduin, S., Clerbaux, C., Camy-Peyret, C., Coheur, P.-F., 2021. Identification of short and long-lived atmospheric trace gases from IASI space observations. Geophys. Res. Lett. 48 (5).

De Visscher, A., 2014. Air dispersion modeling: Foundations and applications. In: Chapter 2: An Air Dispersion Modeling Primer. Wiley, pp. 14–36.

Dise, N.B., Ashmore, M., Belyazid, S., Bleeker, A., Bobbink, R., de Vries, W., Erisman, J.W., Spranger, T., Stevens, C.J., van den Berg, L., 2011. Nitrogen as a threat to European terrestrial biodiversity. In: Sutton, M.A., Howard, C.M., Erisman, J.W., Billen, G., Bleeker, A., Grennfelt, P., van Grinsven, H., Grizzetti, B. (Eds.), The European Nitrogen Assessment. Cambridge University Press, pp. 463–494.

Duncan, B.N., Yoshida, Y., de Foy, B., Lamsal, L.N., Streets, D.G., Lu, Z., Pickering, K.E., Krotkov, N.A., 2013. The observed response of ozone monitoring instrument (OMI) NO_2 columns to NOx emission controls on power plants in the United States: 2005–2011. Atmos. Environ. 81, 102–111.

Ecofys, Fraunhofer Institute for Systems and Innovation Research, Oko-Institut, 2009. Methodology for the Free Allocation of Emission Allowances in EU ETS Post 2012: Sector Report for the Chemical Industry. Technical Report, European Commission.

Erisman, J.W., Galloway, J.N., Dise, N.B., Bleeker, A., Sutton, M.A., Grizzetti, B., Leach, A.M., de Vries, W., 2015. Nitrogen, Too Much of a Vital Resource. Technical Report, WWF Netherlands.

Erisman, J.W., Galloway, J.N., Seitzinger, S., Bleeker, A., Dise, N.B., Petrescu, A.M.R., Leach, A.M., de Vries, W., 2013. Consequences of human modification of the global nitrogen cycle. Philos. Trans. R. Soc. B 368 (1621), 20130116.

Erisman, J.W., Sutton, M.A., Galloway, J., Klimont, Z., Winiwarter, W., 2008. How a century of ammonia synthesis changed the world. Nat. Geosci. 1 (10), 636–639.

European Commission, 2007. Best Available Techniques for the Manufacture of Large Volume Inorganic Chemicals. Technical Report, European Commission.

European Environment Agency, 2019. EMEP/EEA Air Pollutant Emission Inventory Guidbook 2019: Technical Guidance to Prepare National Emission Inventories. techreport 13, European Environment Agency.

European Environment Agency, 2021. Industrial reporting under the industrial emissions directive 2010/75/EU and European pollutant release and transfer register regulation (EC) no 166/2006.

Evangeliou, N., Balkanski, Y., Eckhardt, S., Cozic, A., Van Damme, M., Coheur, P.-F., Clarisse, L., Shephard, M.W., Cady-Pereira, K.E., Hauglustaine, D., 2021. 10-Year satellite-constrained fluxes of ammonia improve performance of chemistry transport models. Atmos. Chem. Phys. 21 (6), 4431–4451.

Fayt, C., Smedt, I.D., Letocart, V., Merlaud, A., Pinardi, G., Roozendael, M.V., 2011. QDOAS. Software User Manual, Brussels, Belgium.

Federal Environmental Agency, 2001. German notes on BAT for the production of large volume solid inorganic chemicals.

Frankenberg, C., Thorpe, A.K., Thompson, D.R., Hulley, G., Kort, E.A., Vance, N., Borchardt, J., Krings, T., Gerilowski, K., Sweeney, C., Conley, S., Bue, B.D., Aubrey, A.D., Hook, S., Green, R.O., 2016. Airborne methane remote measurements reveal heavy-tail flux distribution in Four Corners region. Proc. Natl. Acad. Sci. 113 (35), 9734–9739.

Freney, J., Simpson, J., Denmead, O., 1983. Volatilization of ammonia. In: Freney, J., Simpson, J. (Eds.), Gaseous Loss of Nitrogen from Plant-Soil Systems. Springer, pp. 1–32.

Fujinawa, T., Kuze, A., Suto, H., Shiomi, K., Kanaya, Y., Kawashima, T., Kataoka, F., Mori, S., Eskes, H., Tanimoto, H., 2021. First concurrent observations of NO_2 and CO_2 from power plant plumes by airborne remote sensing. Geophys. Res. Lett. 48 (14).

Galloway, J.N., Townsend, A.R., Erisman, J.W., Bekunda, M., Cai, Z., Freney, J.R., Martinelli, L.A., Seitzinger, S.P., Sutton, M.A., 2008. Transformation of the nitrogen cycle: Recent trends, questions, and potential solutions. Science 320 (5878), 889–892.

Georgoulias, A.K., van der A., R.J., Stammes, P., Boersma, K.F., Eskes, H.J., 2019. Trends and trend reversal detection in 2 decades of tropospheric NO_2 satellite observations. Atmos. Chem. Phys. 19 (9), 6269–6294.

Gifford, F.A.J., 1961. Use of routine meteorological observations for estimating atmospheric dispersion. Nucl. Saf. 2, 47–51.

Gulliver, J.S., 2012. Transport and fate of chemicals in the environment. In: Chapter 5: Chemicals in the Environnement, Turbulent Transport. Springer New York, pp. 89–111.

Hanna, S.R., Briggs, G.A., Hosker, R.P., 1982. Handbook on atmospheric diffusion. In: Chapter 2: Plume Rise. Technical Information Center U. S. Department of Energy, pp. 11–18.

Hersbach, H., Bell, B., Berrisford, P., Hirahara, S., Horanyi, A., Munoz-Sabater, J., Nicolas, J., Peubey, C., Radu, R., Schepers, D., Simmons, A., Soci, C., Abdalla, S., Abellan, X., Balsamo, G., Bechtold, P., Biavati, G., Bidlot, J., Bonavita, M., De Chiara, G., Dahlgren, P., Dee, D., Diamantakis, M., Dragani, R., Flemming, J., Forbes, R., Fuentes, M., Geer, A., Haimberger, L., Healy, S., Hogan, R.J., Holm, E., Janiskova, M., Keeley, S., Laloyaux, P., Lopez, P., Lupu, C., Radnoti, G., de Rosnay, P., Rozum, I., Vamborg, F., Villaume, S., Thépaut, J.-N., 2020. The ERA5 global reanalysis. Q. J. R. Meteorol. Soc. 146 (730), 1999–2049.

Hickman, J.E., Andela, N., Tsigaridis, K., Galy-Lacaux, C., Ossohou, M., Dammers, E., Damme, M.V., Clarisse, L., Bauer, S.E., 2021. Continental and ecoregion-specific drivers of atmospheric NO_2 and NH_3 seasonality over Africa revealed by satellite observations. Glob. Biogeochem. Cycles 35.

Hulley, G.C., Duren, R.M., Hopkins, F.M., Hook, S.J., Vance, N., Guillevic, P., Johnson, W.R., Eng, B.T., Mihaly, J.M., Jovanovic, V.M., Chazanoff, S.L., Staniszewski, Z.K., Kuai, L., Worden, J., Frankenberg, C., Rivera, G., Aubrey, A.D., Miller, C.E., Malakar, N.K., Tomas, J.M.S., Holmes, K.T., 2016. High spatial resolution imaging of methane and other trace gases with the airborne Hyperspectral Thermal Emission Spectrometer (HyTES). Atmos. Meas. Tech. 9 (5), 2393–2408.

IL & FS Ecosmart Limited, 2010. Technical EIA Guidance Manual for Soda Ash Industry. Technical Report, The Ministry of Environment and Forests.

Jacob, D.J., Varon, D.J., Cusworth, D.H., Dennison, P.E., Frankenberg, C., Gautam, R., Guanter, L., Kelley, J., McKeever, J., Ott, L.E., Poulter, B., Qu, Z., Thorpe, A.K., Worden, J.R., Duren, R.M., 2022. Quantifying methane emissions from the global scale down to point sources using satellite observations of atmospheric methane. Atmos. Chem. Phys. 22 (14), 9617–9646.

Kharol, S.K., Shephard, M.W., McLinden, C.A., Zhang, L., Sioris, C.E., O'Brien, J.M., Vet, R., Cady-Pereira, K.E., Hare, E., Siemons, J., Krotkov, N.A., 2018. Dry deposition of reactive nitrogen from satellite observations of ammonia and nitrogen dioxide over North America. Geophys. Res. Lett. 45 (2), 1157–1166.

Kneizys, F.X., Abreu, L.W., Anderson, G.P., Chetwynd, J.H., Shettle, E.P., Berk, A., Bernstein, L.S., Robertson, D.C., Acharya, P., Rothman, L.S., Selby, J.E.A., Gallery, W.O., Clough, S.A., 1996. The MODTRAN 2/3 Report and LOWTRAN 7 MODEL. Technical Report, Phillips Laboratory, Geophysics Directorate.

Kowatsch, S., 2010. Mineral wool insulation binders. In: Phenolic Resins: A Century of Progress. Springer Berlin Heidelberg, pp. 209–242.

Kuai, L., Kalashnikova, O.V., Hopkins, F.M., Hulley, G.C., Lee, H., Garay, M.J., Duren, R.M., Worden, J.R., Hook, S.J., 2019. Quantification of ammonia emissions with high spatial resolution thermal infrared observations from the hyperspectral thermal emission spectrometer (HyTES) airborne instrument. IEEE J. Sel. Top. Appl. Earth Obs. Remote Sens. 12 (12), 4798–4812.

Lagueux, P., Farley, V., Rolland, M., Chamberland, M., Puckrin, E., Turcotte, C.S., Lahaie, P., Dube, D., 2009a. Airborne measurements in the infrared using FTIR-based imaging hyperspectral sensors. In: 2009 First Workshop on Hyperspectral Image and Signal Processing: Evolution in Remote Sensing. pp. 1–4.

Lagueux, P., Farleya, V., Chamberland, M., Villemaire, A., Turcotte, C., Puckrinb, E., 2009b. Design and Performance of the Hyper-Cam, an Infrared Hyperspectral Imaging Sensor. Defense Technical Information Center.

Lelieveld, J., Evans, J.S., Fnais, M., Giannadaki, D., Pozzer, A., 2015. The contribution of outdoor air pollution sources to premature mortality on a global scale. Nature 525 (7569), 367–371.

Manolakis, D., Lockwood, R., Cooley, T., 2016. Hyperspectral Imaging Remote Sensing: Physics, Sensors, and Algorithms. Cambridge University Press.

Martin, D.O., 1976. Comment on the change of concentration standard deviations with distance. J. Air Pollut. Control Assoc. 26 (2), 145–147.

McLinden, C.A., Fioletov, V., Shephard, M.W., Krotkov, N., Li, C., Martin, R.V., Moran, M.D., Joiner, J., 2016. Space-based detection of missing sulfur dioxide sources of global air pollution. Nat. Geosci. 9 (7), 496–500.

Meier, A.C., Schönhardt, A., Bösch, T., Richter, A., Seyler, A., Ruhtz, T., Constantin, D.-E., Shaiganfar, R., Wagner, T., Merlaud, A., Roozendael, M.V., Belegante, L., Nicolae, D., Georgescu, L., Burrows, J.P., 2017. High-resolution airborne imaging DOAS measurements of NO_2 above Bucharest during AROMAT. Atmos. Meas. Tech. 10 (5), 1831–1857.

Merlaud, A., Belegante, L., Constantin, D.-E., Hoed, M.D., Meier, A.C., Allaart, M., Ardelean, M., Arseni, M., Bösch, T., Brenot, H., Calcan, A., Dekemper, E., Donner, S., Dörner, S., Dragomir, M.C.B., Georgescu, L., Nemuc, A., Nicolae, D., Pinardi, G., Richter, A., Rosu, A., Ruhtz, T., Schönhardt, A., Schuettemeyer, D., Shaiganfar, R., Stebel, K., Tack, F., Vâjâiac, S.N., Vasilescu, J., Vanhamel, J., Wagner, T., Van Roozendael, M., 2020. Satellite validation strategy assessments based on the AROMAT campaigns. Atmos. Meas. Tech. 13 (10), 5513–5535.

Merlaud, A., Tack, F., Constantin, D., Georgescu, L., Maes, J., Fayt, C., Mingireanu, F., Schuettemeyer, D., Meier, A.C., Schönardt, A., Ruhtz, T., Bellegante, L., Nicolae, D., Hoed, M.D., Allaart, M., Van Roozendael, M., 2018. The small whiskbroom imager for atmospheric composition monitoring (SWING) and its operations from an unmanned aerial vehicle (UAV) during the AROMAT campaign. Atmos. Meas. Tech. 11 (1), 551–567.

Montembeault, Y., Lagueux, P., Farley, V., Villemaire, A., Gross, K.C., 2010. Hyper-cam: Hyperspectral IR imaging applications in defence innovative research. In: 2010 2nd Workshop on Hyperspectral Image and Signal Processing: Evolution in Remote Sensing. pp. 1–4.

Pasquill, F., 1961. The estimation of the dispersion of wind-borne material. Meteorol. Mag. 90, 33–49.

Paulot, F., Jacob, D.J., Pinder, R.W., Bash, J.O., Travis, K., Henze, D.K., 2014. Ammonia emissions in the United States, European union, and China derived by high-resolution inversion of ammonium wet deposition data: Interpretation with a new agricultural emissions inventory (MASAGE_NH3). J. Geophys. Res.: Atmos. 119 (7), 4343–4364.

Pinterits, M., Anys, M., Gager, M., Ullrich, B., 2020. European Union Emission Inventory Report 1990-2018 under the UNECE Convention on Long-Range Transboundary Air Pollution. Technical Report, LRTAP, European Environment Agency.

Platt, U., Stutz, J., 2008. Differential Optical Absorption Spectroscopy: Principles and Applications. Springer Verlag.

Pope, C.A., Ezzati, M., Dockery, D.W., 2009. Fine-particulate air pollution and life expectancy in the United States. New Engl. J. Med. 360 (4), 376–386.

Rodgers, C.D., 2000. Inverse Methods for Atmospheric Sounding: Theory and Practice. World Scientific.

Seinfeld, J.H., Pandis, S.N., 2016. Atmospheric chemistry and physics : From air pollution to climate change. In: Chapter Atmospheric Trace Constituents, third ed. Wiley, pp. 18–65.

Shaiganfar, R., Beirle, S., Sharma, M., Chauhan, A., Singh, R.P., Wagner, T., 2011. Estimation of NO_x emissions from Delhi using Car MAX-DOAS observations and comparison with OMI satellite data. Atmos. Chem. Phys. 11 (21), 10871–10887.

Shephard, M.W., Dammers, E., Cady-Pereira, K.E., Kharol, S.K., Thompson, J., Gainariu-Matz, Y., Zhang, J., McLinden, C.A., Kovachik, A., Moran, M., Bittman, S., Sioris, C.E., Griffin, D., Alvarado, M.J., Lonsdale, C., Savic-Jovcic, V., Zheng, Q., 2020. Ammonia measurements from space with the cross-track infrared sounder: characteristics and applications. Atmos. Chem. Phys. 20 (4), 2277–2302.

Souri, A.H., Choi, Y., Pan, S., Curci, G., Nowlan, C.R., Janz, S.J., Kowalewski, M.G., Liu, J., Herman, J.R., Weinheimer, A.J., 2018. First top-down estimates of anthropogenic NO_2 emissions using high-resolution airborne remote sensing observations. J. Geophys. Res.: Atmos. 123 (6), 3269–3284.

Spurr, R., 2008. LIDORT and VLIDORT: Linearized pseudo-spherical scalar and vector discrete ordinate radiative transfer models for use in remote sensing retrieval problems. In: Light Scattering Reviews, Vol. 3. Springer Berlin Heidelberg.

Stavrakou, T., Müller, J.F., Boersma, K.F., van der A, R.J., Kurokawa, J., Ohara, T., Zhang, Q., 2013. Key chemical NO_x sink uncertainties and how they influence top-down emissions of nitrogen oxides. Atmos. Chem. Phys. 13 (17), 9057–9082.

Steinhauser, G., 2008. Cleaner production in the solvay process: general strategies and recent developments. J. Clean. Prod. 16 (7), 833–841.

Stockie, J.M., 2011. The mathematics of atmospheric dispersion modeling. SIAM Rev. 53 (2), 349–372.

Sutton, M.A., Reis, S., Riddick, S.N., Dragosits, U., Nemitz, E., Theobald, M.R., Tang, Y.S., Braban, C.F., Vieno, M., Dore, A.J., Mitchell, R.F., Wanless, S., Daunt, F., Fowler, D., Blackall, T.D., Milford, C., Flechard, C.R., Loubet, B., Massad, R., Cellier, P., Personne, E., Coheur, P.F., Clarisse, L., Van Damme, M., Ngadi, Y., Clerbaux, C., Skjoth, C.A., Geels, C., Hertel, O., Kruit, R.J.W., Pinder, R.W., Bash, J.O., Walker, J.T., Simpson, D., Horvath, L., Misselbrook, T.H., Bleeker, A., Dentener, F., de Vries, W., 2013. Towards a climate-dependent paradigm of ammonia emission and deposition. Philos. Trans. R. Soc. B 368.

Tack, F., Merlaud, A., Iordache, M.-D., Pinardi, G., Dimitropoulou, E., Eskes, H., Bomans, B., Veefkind, P., Van Roozendael, M., 2021. Assessment of the TROPOMI tropospheric NO_2 product based on airborne APEX observations. Atmos. Meas. Tech. 14 (1), 615–646.

Tack, F., Merlaud, A., Meier, A.C., Vlemmix, T., Ruhtz, T., Iordache, M.-D., Ge, X., van.der Wal, L., Schuettemeyer, D., Ardelean, M., Calcan, A., Constantin, D., Schönhardt, A., Meuleman, K., Richter, A., Van Roozendael, M., 2019. Intercomparison of four airborne imaging DOAS systems for tropospheric NO_2 mapping – the AROMAPEX campaign. Atmos. Meas. Tech. 12 (1), 211–236.

Telops, 2022. Hyperspectral IR cameras. consulted on 24/08/2022.

Theys, N., Campion, R., Clarisse, L., Brenot, H., van Gent, J., Dils, B., Corradini, S., Merucci, L., Coheur, P.-F., Van Roozendael, M., Hurtmans, D., Clerbaux, C., Tait, S., Ferrucci, F., 2013. Volcanic SO_2 fluxes derived from satellite data: A survey using OMI, GOME-2, IASI and MODIS. Atmos. Chem. Phys. 13 (12), 5945–5968.

Tratt, D.M., Buckland, K.N., Young, S.J., Johnson, P.D., Riesz, K.A., Molina, K.C., 2013. Remote sensing visualization and quantification of ammonia emission from an inland seabird colony. J. Appl. Remote Sens. 7 (1), 073475.

Tratt, D.M., Young, S.J., Johnson, P.D., Buckland, K.N., Lynch, D.K., 2016. Multi-year study of remotely-sensed ammonia emission from fumaroles in the salton sea geothermal field. In: 2016 8th Workshop on Hyperspectral Image and Signal Processing: Evolution in Remote Sensing (WHISPERS). IEEE, pp. 1–5.

Tratt, D.M., Young, S.J., Lynch, D.K., Buckland, K.N., Johnson, P.D., Hall, J.L., Westberg, K.R., Polak, M.L., Kasper, B.P., Qian, J., 2011. Remotely sensed ammonia emission from fumarolic vents associated with a hydrothermally active fault in the Salton Sea Geothermal Field, California. J. Geophys. Res.: Atmos. 116 (D21).

Van Damme, M., Clarisse, L., Franco, B., Sutton, M.A., Erisman, J.W., Kruit, R.W., Zanten, M.van., Whitburn, S., Hadji-Lazaro, J., Hurtmans, D., Clerbaux, C., Coheur, P.-F., 2021. Global, regional and national trends of atmospheric ammonia derived from a decadal (2008–2018) satellite record. Environ. Res. Lett. 16 (5), 055017.

Van Damme, M., Clarisse, L., Whitburn, S., Hadji-Lazaro, J., Hurtmans, D., Clerbaux, C., Coheur, P.-F., 2018. Industrial and agricultural ammonia point sources exposed. Nature 564 (7734), 99–103.

Varon, D.J., Jacob, D.J., McKeever, J., Jervis, D., Durak, B.O.A., Xia, Y., Huang, Y., 2018. Quantifying methane point sources from fine-scale satellite observations of atmospheric methane plumes. Atmos. Meas. Tech. 11 (10), 5673–5686.

Wang, R., Guo, X., Pan, D., Kelly, J.T., Bash, J.O., Sun, K., Paulot, F., Clarisse, L., Van Damme, M., Whitburn, S., Coheur, P.-F., Clerbaux, C., Zondlo, M.A., 2021. Monthly patterns of ammonia over the contiguous United States at 2-km resolution. Geophys. Res. Lett. 48 (5).

Whitburn, S., Van Damme, M., Clarisse, L., Bauduin, S., Heald, C.L., Hadji-Lazaro, J., Hurtmans, D., Zondlo, M.A., Clerbaux, C., Coheur, P.-F., 2016. A flexible and robust neural network IASI-NH_3 retrieval algorithm. J. Geophys. Res.: Atmos. 121 (11), 6581–6599.

Willis, G.E., Deardorff, J.W., 1983. On plume rise within a convective boundary layer. Atmos. Environ. 17 (12), 2435–2447.

Zhang, X., Wu, Y., Liu, X., Reis, S., Jin, J., Dragosits, U., Van Damme, M., Clarisse, L., Whitburn, S., Coheur, P.-F., Gu, B., 2017. Ammonia emissions may be substantially underestimated in China. Environ. Sci. Technol. 51 (21), 12089–12096.